De novo design of high-affinity single-domain antibodies

Rob van der Kant*[,1,2,3], Zhongyao Zhang*[,1,2,3,4], Iva Marković[5,6], David Vizarraga[7], Teresa Garcia[1,2,3], Katerina Maragkou[1,2,3], Javier Delgado Blanco[7], Damiano Cianferoni[7], Gabriele Orlando[1,2,3], Carlo Carolis[7], Alexander N. Volkov[10,11], Savvas N. Savvides[5,6], Maarten Dewilde[4,12], Joost Schymkowitz[#,1,2,3], Luis Serrano Pubul[#,7,8,9], Frederic Rousseau[#,1,2,3]

*These authors contributed equally to this work.

To whom correspondence should addressed: joost.schymkowitz@kuleuven.be, luis.serrano@crg.es, Frederic.rousseau@kuleuven.be

[1]Switch Laboratory, VIB Center for Brain and Disease Research, VIB; Leuven, 3000, Belgium.

[2]Switch Laboratory, Department of Cellular and Molecular Medicine, KU Leuven; Leuven, 3000, Belgium.

[3]Switch Laboratory, VIB Center for AI & Computational Biology, VIB; Leuven, 3000, Belgium.

[4]Laboratory for Therapeutic and Diagnostic Antibodies, Department of Pharmaceutical and Pharmacological Sciences, KU Leuven; Leuven, 3000, Belgium.

[5]Unit for Structural Biology, Department of Biochemistry and Microbiology, Ghent University; Ghent, 9052, Belgium.

[6]Unit for Structural Biology, VIB-UGent Center for Inflammation Research; Ghent, 9052, Belgium.

[7]Centre for Genomic Regulation (CRG), The Barcelona Institute of Science and Technology; Barcelona, 08003, Spain.

[8]Universitat Pompeu Fabra (UPF); Barcelona, 08002, Spain.

[9]ICREA; Barcelona, 08010, Spain.

[10]VIB- VUB Center for Structural Biology; Brussels, 1050, Belgium.

[11]Jean Jeener NMR Centre, Vrije Universiteit Brussel (VUB); Brussels, 1050, Belgium.

[12]PharmAbs, the KU Leuven Antibody Center, KU Leuven; Leuven, 3000, Belgium.

Abstract

Developing antibodies is complex and resource-intensive, and methods for designing antibodies targeting specific epitopes are lacking. We introduce a *de novo* antibody design approach leveraging the empirical force field FoldX to design complementarity determining regions (CDRs). Starting from a scaffold VHH, we tackled three challenges of increasing difficulty: 1) design the CDRs to optimize VHH stability and affinity for its original target; 2) design the CDRs for high affinity to the human ortholog; 3) design the CDRs for low nanomolar affinity for a pre-defined epitope on the unrelated human Interleukin-9 receptor alpha, for which no antibodies were previously developed. For each challenge we reached single digit nanomolar affinity in a single design cycle. Our approach allows *de novo* design of high-affinity VHHs while ensuring specificity and stability.

Introduction

Antibody-based therapeutics have emerged as highly promising tools for targeting specific molecular entities. Their remarkable ability to bind a wide range of molecules makes them candidates for treating a wide spectrum of diseases, ranging from infectious diseases (*1*) to cancer (*2*). Over the last decade, the majority of biologic license applications approved by the FDA are therapeutic antibodies (*3*). Traditional methodologies for antibody discovery, rooted in animal immunizations, hybridoma technologies, and phage display, have been crucially important to establish the potential and positioning of antibody-based therapeutics. However, these approaches are fraught with fundamental challenges such as suboptimal developability, limited and unpredictable cross-reactivity of the developed antibodies, and difficulties in targeting conserved binding epitopes (*4, 5*). Furthermore, ethical concerns regarding the use of animal models for immunization pose additional hurdles (*6*). These limitations necessitate a paradigm shift towards innovative approaches to address the evolving demands of antibody development. Indeed, recent efforts have led to deep learning networks and diffusion-based generative approaches to design novel antibody sequences, however the *de novo* design of antibodies without a base remains largely unexplored (*7-10*).

In this context, structure-based *de novo* antibody design has emerged as a promising approach, leveraging computational methods to predict and optimize antibody-antigen interactions (*5, 11-15*). Central to this approach is the ability to accurately model the three-dimensional structure of antibodies and their target antigens, allowing for rational design and optimization of binding interfaces (*13, 14*). Through a combination of computational molecular docking, sequence optimization, and experimental validation of the designed models, structure-based *de novo* antibody design holds the potential to streamline the antibody development process and to facilitate the discovery of antibodies with tailor-made properties such as enhanced binding affinity and stability (*14, 15*).

We approach structure-based *de novo* antibody design through two main *in silico* steps. Firstly, a molecular docking step is performed to bring a template antibody in proximity to a predefined epitope, and secondly, a design step, where the sequence is built that can accommodate binding to the epitope while retaining foldability of the antibody in isolation. The latter step can be validated by removing the sequence information from a known complex of an antibody bound to a protein ligand and evaluating if it is possible to design sequences that are able to bind the same epitope, termed re-paratoping. Here we report an *in silico* antibody design pipeline, termed EvolveX, for the generation of antibodies targeting predefined epitopes. The EvolveX pipeline addresses the main *in silico* issues in *de novo* design of antibodies against a predefine target: Docking of the antibody on the target, optimization of the structure of the bound antibody and designing of the sequence of the complementarity determining regions of the antibody (CDRs), while maintaining good thermodynamic stability of the antibody and avoiding the introduction of aggregation propensity. Structure optimization is achieved using ModelX (*16-18*), interaction energy and antibody stability are evaluated by the empirical forcefield FoldX (*18, 19*) and aggregation propensity by TANGO (*20-22*). The efficacy of the antibody design step is validated through a series of experimental assays, including phage display, biophysical characterization, NMR and X-ray crystallography, demonstrating the successful design of VHHs starting from both

high and low-affinity protein complexes (*23*). We further explored the flexibility of the EvolveX pipeline by re-designing the template VHH towards an unrelated protein target, the human Interleukin-9 receptor alpha (hIL-9Rα) interface, obtaining binders with low nanomolar affinity in one design cycle. Overall, our finding underscores the potential of structure-based *de novo* antibody design as a powerful tool in biotechnology and drug discovery.

Results

In silico rebuilding of an antibody paratope starting from a high affinity complex

Wen et al. (*23*) generated a VHH, Nb119 (in this work further referred to as VHH_WT), through classical immunization against the extracellular IgV domain of the mouse Vsig4 protein. This VHH showed high affinity towards mouse Vsig4 (mVsig4, K_D ~5 nM), but a thousand-fold lower affinity towards human Vsig4 (hVsig4, K_D ~5 µM). The structure of the antibody-antigen complex was determined by X-ray crystallography for both orthologs. We used the crystal structure of the complex of the VHH to mVsig4 (VHH_WT-mVsig4, PDBID: 5IMM and 5IMO, (*23*)) to validate the capacity of EvolveX to rebuild an antibody paratope starting from a high affinity complex (Fig. 1A). To this end, we removed the sequence information from CDR2 and CDR3 of the VHH_WT-mVsig4 complexes since these regions are most involved in binding to mVsig4: Each amino acid residue in CDR2 and CDR3 (except Proline and Glycine) that resided within 8 Å from the ligand was mutated to Alanine. From this all-alanine starting point, the compatibility of each of the selected positions with all 20 amino acids was explored using the *PSSM* function in FoldX, which yields the impact of each point mutation on both the thermodynamic stability of the VHH, as well as interaction energy with the ligand (see methods for details). Based on these numbers, random starting sequences were generated to be compatible with the complex structure. These starting sequences were used as input for a genetic algorithm, where selection was based on the interaction energy computed by FoldX, with preset ceilings for the thermodynamic stability of the VHH (see Fig. 1A and methods for details).

The resulting sequences were filtered based on thresholds for the FoldX prediction of interaction energy and VHH stability (*19*), as well as TANGO predicted aggregation propensity (*20*). Additionally, Z-scores were calculated based on densities derived from publicly available crystal structures of VHHs bound to protein ligands, for cavities within the VHH, cavities at the interface of VHHs with their ligand and VHH net charge (see methods for details). The top 6000 sequences with the lowest summed Z-scores were obtained as oligonucleotides and cloned into the VHH_WT backbone in a phagemid vector. The resulting library was enriched for mVsig4 binders through several rounds of phage display using progressively lower concentrations of mVsig4 down to 5 nM (see fig S1 and methods for details). Periplasmic extracts were prepared for 188 randomly picked VHH clones from the enriched libraries, yielding 36 unique sequences (table S1), and subsequently analyzed for mVsig4 binding using the Amplified Luminescent Proximity Homogenous Assay (AlphaScreen) (Fig. 1B). This revealed clones with AlphaScreen signal to noise ratios (S/N ratio) similar- or higher than VHH_WT, of which 12 were selected. Of these VHH variants, we determined the dissociation velocity rate constant governing dissociation from

mVsig4 (k_d) using BioLayer Interferometry (BLI) (Fig. 1C, table S2), which was quite similar in all cases.

The top four candidates (VHH_m1, VHH_m2, VHH_m3, and VHH_m4) with slightly more favorable k_d values than the rest were subsequently recombinantly produced at larger scale (10 mg), chromatographically purified, and biophysically characterized. Binding affinities (K_D) for mVsig4 were determined using Surface Plasmon Resonance (SPR) (Fig. 1D and E, fig S3) and BLI (Fig. 1E, fig S2), revealing that the four VHH candidates have affinities close to VHH_WT (Fig. 1E). The four VHHs were subjected to chemical denaturation analysis using urea and guanidine hydrochloride (fig S4). Curve fitting indicated a significant increase in stability by about -2 kcal/mol for all four designed sequences (Fig. 1F) compared to VHH_WT. Thermal protein unfolding (T_m) and aggregation onset temperatures (T_{agg}) were determined simultaneously using Intrinsic Tryptophan Fluorescence (ITF) (Fig. 1G, fig S5) and Right-Angle Light Scattering (RALS), respectively (Fig. 1H, fig S6). The designed sequences showed increased thermal stability, about 5 °C in both T_m and T_{agg}, and the relative order in stability coincides quite well between the chemical and thermodynamic denaturation with VHH_m4 being the more stable and VHH_m3 the least.

Although EvolveX computationally explored 5 positions in CDR2 and 12 in CDR3 (~$1x10^{22}$ theoretical combinations), the four selected candidates were very similar to each other in sequence, differing only at two positions where we found chemically similar amino acids: a Tyr or Phe at position 107 and an Asp or a Glu at position 112, respectively (Fig. 1I, table S3). Interestingly the two more stable VHH sequences VHH_m2 and VHH_m4 contain a Glu at position 112, while having a Phe or a Tyr at position 107 does not seem to have an important role in stability. Compared to wild type, the designed variants carried two mutations in the CDR2 loop and 5 or 6 mutations in the CDR3 loop (Fig. 1I).

The successful identification of the multi-parametric optimized sequences with EvolveX demonstrates the capability of our computational method in designing VHH CDR sequence combinations when starting from a structure of a high affinity complex.

In silico design of optimal CDR2/3 sequences targeting human Vsig4

Subsequently, we set out to identify high-affinity binders starting from a low-affinity complex, starting from structural templates obtained from the crystal structures of the low micromolar affinity complex between VHH_WT and human Vsig4 (PDB ID 5IMK and 5IML, (*23*)) (Fig. 2A). The backbone conformation of CDR3 was adapted using the *Bridging* command in ModelX (*18*) using 5IMK as a starting point, adding 14 starting complex structures (see methods for details). Sequence design as described above yielded 6000 candidate sequences (Fig. 2A). The mouse VHH_m and human VHH_h sequences were combined into one phage library, which was selected against hVsig4 using similar procedures as before (fig S1). Based on the enrichment, the phages from the third round of selection with 50nM hVsig4 (R3) and round 4 selection with 5nM hVsig4 (R4) were chosen for screening. We randomly picked 188 colonies from both libraries for expression and sequencing, yielding 112 unique sequences, which we ranked for binding to hVsig4 using classical ELISA. The average ELISA signal from the R4_hVsig4_5nM group is higher

than that of the R3_hVsig4_50nM group and most of the clones have a higher ELISA signal than VHH_WT (Fig. 2B, table S4). 56 sequences were tested for off-rate using BLI (Fig. 2C, table S5). The 3 clones with the best off-rates (VHH_h1, VHH_h2 and VHH_h3), the clone with the highest ELISA signal (VHH_h4), and the most occurring clone (VHH_h5) were selected for purification and subsequent biophysical characterization.

Remarkably, the measured affinity of the designed sequences situated in the low nanomolar affinities (Fig. 2D and E), meaning an improvement in affinity to human Vsig4 of up to 1000-fold over VHH_WT (Fig. 2D and E, fig S7, fig S8). Affinities were cross validated with the VHH_m hits for binding to both mVsig4 and hVsig4. This revealed all designed VHHs show specificity for their intended target (fig S9). All VHHs were subjected to chemical and thermal denaturation. Chemical denaturation by urea (fig S10A) and guanidine hydrochloride (fig S10B) indicated the five designed sequences had an increase in stability from -1.5 up to -3.5 kcal/mol compared with the original human VHH_WT (Fig. 2F and table S6). Both T_m (Fig. 2G, fig S11) and T_{agg} (Fig. 2H, fig S12) were significantly improved for all designed sequences compared to human VHH_WT (table S6).

VHH_h2, VHH_h4 and VHH_h5 exhibited the strongest binding to hVsig4 (K_D_BLI and K_D_SPR ~ 5 nM), which is 1000-fold better than VHH_WT (K_D_BLI ~ 5 µM) (Fig. 2E, table S6). VHH_h1 and VHH_h3 exhibited worse K_D values (10~40nM) to hVsig4 than the first three candidates, while still being substantially better than VHH_WT. In all cases we found common mutations among the five VHHs (WN to PF in CDR2, DK to NR, F to D and E to N in CDR3) (Fig. 2I). Interestingly, when comparing the sequences analyzed for hVsig4 and mVsig4, we found some positions that were mutated (although to different residues) in both cases at CDR2 (GS) and CDR3 (D and E). In the case of the hVsig4 we found more positions that were mutated indicating the need of larger sequence changes to ensure high affinity binding.

To confirm the epitope and evaluate the predictions done by EvolveX, the designed VHHs were crystallized in complex with hVsig4 (Fig. 3, fig S13, table S7). All five high-resolution crystal structures revealed that the binding epitope is almost identical among all hit VHHs compared to the crystal structure of VHH_WT (Fig. 3B and C). When superimposing on hVsig4 we see that the orientation for each VHH as well as for VHH_WT binds is slightly different (Fig. 3B and fig S14). This might be due to the interaction between the designed negative charges in CDR3 (Asp107 and Asp109) and the N-terminus of hVsig4 (fig S14D). Overall, more residues are interacting with hVsig4 in the designed VHHs compared to VHH_WT (table S8). Additionally, the conformation of CDR3 is very similar to the VHH_WT crystal structures (mean pairwise backbone RMSD = 0.29 Å) (Fig. 3C).

To elucidate the biophysical parameters responsible for the increased stability of the designed sequences over the original VHH, we studied VHH_WT and VHH_h4 (the most stable binder to hVsig4) by nuclear magnetic resonance (NMR) spectroscopy. VHH_WT features a well-dispersed heteronuclear single-quantum correlation (HSQC) spectrum, where nearly all peaks could be unambiguously assigned (fig S15). Interestingly, most residues in the three CDRs showed no backbone amide resonances (fig S16). The paucity of the CDR signals was reported before for several other VHHs and attributed to a pronounced flexibility and conformational heterogeneity of the CDR loops (*24-26*). The HSQC spectrum of VHH_h4 is similar to that of VHH_WT, but contains more peaks (fig S17), some of which could be assigned to the residues in the CDR3 loop

(fig S18). In addition, several VHH_h4 resonances not observed in the NMR spectra of the VHH_WT (and showing very weak signals in triple-resonance NMR experiments, precluding their unambiguous assignment) could belong to other CDRs. Overall, it appears that VHH_h4 undergoes a much less extensive conformational exchange upon target binding than the WT. Predicted from the backbone chemical shifts, the secondary structures of VHH_WT and VHH_h4 are very similar and agree well with that seen in the X-ray structure (fig S16 and S18), which testifies to the high structural conservation of the VHH fold outside the CDRs. To delve further into differences between VHH_WT and VHH_h4, we performed NMR relaxation analysis (fig S19, S20 and S21), which revealed that free VHH_h4 in solution maintains the bound-like protein conformation, with closely packed CDR loops undergoing limited motion. At the same time, the CDRs of VHH_WT are largely disordered and involved in extensive conformational exchange. These differences could explain the observed disparity in the thermal stability of the two proteins, where motional disorder of CDRs renders VHH_WT less stable.

In silico design pipeline for the *de novo* design of antibodies against defined targets

A much bigger challenge in antibody design is the *de novo* design of a single domain or full-length antibody against a defined epitope, since this involves docking of antibody scaffold onto the antigen, remodeling the loops and search for sequences that mediate high affinity binding. A docking method based on hotspot grafting was developed to dock VHH templates onto predefined epitope sidechains overlapping with the intended interface. The docking method places a template VHH near the epitope of choice as well as ensure that at least some of the interactions between the antibody and the hotspot residue are grafted simultaneously. All crystal structures of complexes between VHHs and protein ligands are first analyzed using FoldX to identify which amino acids on the epitope are predicted to contribute most to the interaction, termed hotspot residues. These hotspot residue sidechains are varied by modelling the energetically likely rotamers using the *Rotacloud* command in FoldX. The hotspot database is then used to dock template VHHs onto the amino acids in the predefined epitope of the target protein.

Validation of our *de novo* design pipeline by targeting human Interleukin-9 receptor alpha

To validate our approach, we selected as a target the crystal structure (PDB ID 7OX5, (*27*)) and AlphaFold models (Q01113, (*28*)) of human Interleukin-9 receptor alpha (IL-9Rα). For *de novo* design, an epitope was selected in the stem region of hIL-9Rα proximal to the membrane domain where the receptor would be expected to interact with the equivalent stem region of the Interleukin-2 receptor gamma (γcR/IL-2Rγ) and outside of the hIL-9 binding site. Antibody binding at this interface would be expected to inhibit IL-9 downstream signaling, which could be a therapeutically beneficial approach in asthma and generally atopic diseases where IL-9 is seen as one of the key players in disease severity (*29*).

The 1.2M docks resulting from the hot-spot residue docking approach described above were filtered based on number of interacting residues and backbone clashes, leaving 900 docks. These docks were grouped by hotspot residue and template structure, leaving 15 groups of docks. Representative docks for each group were visually inspected for viability, judging was done based

on CDRs involved, VHH orientation, interaction potential and proximity to glycosylation sites. Interestingly, among the groups of docks that met our criteria, 72 different docks coincidentally used VHH_WT bound to hVsig4 as a template. We then selected this VHH_WT as our starting model to close the design process showing we could redesign a VHH against a target keeping the K_D and improving physical properties, increase affinity against an ortholog of the target, and finally and more challengingly modify it to recognize a completely unrelated target. Ile111 of hVsig4 in complex with VHH_WT was superimposed on different conformations of Ile208 on structural models of hIL-9Rα. This group was used as a starting point for the antibody design effort. The same sequence design method as with the mouse and human Vsig4 complexes was used for these docked templates, except here all three CDRs were explored simultaneously instead of only CDR2 and CDR3. As in the mVsig4 case, the backbone conformation of the CDRs was not adapted for the 72 starting complexes (Fig. 4A).

The top 16477 sequences with the lowest summed Z-scores were ordered as an oligo pool. Two phagemid libraries were created, one ensuring a low recombination rate and one allowing full recombination between all CDRs. Both libraries were selected for binding to hIL-9Rα using several rounds of phage display (fig S22). Based on the enrichment, the phages from selection rounds with 50nM or 5 nM hIL-9Rα were chosen for both low and high recombination rate libraries (Fig. 4B). VHH sequences from these four groups were recloned in pool into an expression vector and transformed into TG1 bacteria. Likewise, 570 colonies were randomly picked for expression and screening, consisting of 122 unique sequences. The average AlphaScreen signals are comparable between the low and high recombination libraries (Fig. 4B). 30 sequences were tested for off-rate using BLI (Fig. 4C). 8 sequences were selected for purification and biophysical characterization based on off-rates and AlphaScreen signals. Of these, seven turned out to have affinities below 25 nM, the best hit VHH showed a 1.3 nanomolar affinity to hIL-9Rα and the worst had an affinity of 43 nM (Fig. 4D and E, fig S23). To test whether the hits with *de novo* designed sequences bind specifically to hIL-9Rα, AlphaScreen was performed for hIL-9Rα, hVsig4 and mVsig4. This showed all sequences that bind hIL-9Rα do not bind to either hVsig4 or mVsig4 (Fig. 4F). Additionally, VHH_WT does not show any AlphaScreen signal for hIL-9Rα. Our highest affinity hit showed a T_m of 83 degrees C (Fig. 4G).

Discussion

The advent of computational methods for antibody design is revolutionizing the field, allowing for the targeted creation of antibodies with specific binding capabilities and stability. In this study, we demonstrate the efficacy of an *in silico* antibody design pipeline, EvolveX, in designing VHHs targeting predefined epitopes on protein targets. Our results highlight the versatility and robustness of the approach, as evidenced by successful sequence design efforts starting from both high and low-affinity complexes, as well as targeting a novel protein interface.

The success of the *in silico* antibody design pipeline is underscored by the validation experiments conducted for both high and low-affinity complexes of VHH_WT with mouse and human Vsig4, respectively. Through a combination of sequence and structure optimization, and biophysical and

structural experimental validation, EvolveX was able to design small, targeted libraries yielding high-affinity VHHs. Notably, the designed VHHs consistently exhibited significantly enhanced thermal, colloidal, and chemical stability, indicating the robustness of the computational design process.

Furthermore, our approach extends beyond known protein complexes, as demonstrated by the successful design of VHHs targeting the membrane-proximal region of hIL-9Rα. By employing a novel docking method, leveraging a database of hotspot residues derived from crystal structures of antibody-ligand complexes, we were able to design VHHs with high affinity for hIL-9Rα. Additionally, the top hits were designed based on AlphaFold models of hIL-9Rα, allowing *de novo* design against epitopes for which experimental structures are lacking. This represents a significant advancement, as it showcases the capability of our computational framework to design antibodies targeting novel protein epitopes without relying on structural data of an existing antibody-antigen complex.

The designed VHHs exhibited not only high affinity but also demonstrated thermodynamic stability comparable to or better than the wild-type antibody. Structural analysis of the VHH-hVsig4 protein complexes confirmed epitope retention and revealed insights into the binding mechanism, providing valuable information for further optimization and development.

Interestingly, comparison of the designed VHHs targeting mouse and human Vsig4 revealed differences in the mutation patterns within the complementarity-determining regions (CDRs), indicating the need for tailored design strategies depending on the target species.

Collectively, our study demonstrates the power of computational antibody design in generating VHHs with desired binding properties. The combination of molecular modeling, sequence optimization, and experimental validation offers a systematic and efficient approach for antibody engineering, with broad implications for drug development, diagnostics, and biotechnology. Future work will focus on further refining the design pipeline, reducing library sizes and exploring its application to additional protein targets and therapeutic modalities.

Methods summary

A detailed description of the dataset curation, modeling of biological inputs, data pipeline, *in silico* design methods, and experimental validation can be found in the **Supplementary Materials and Methods**.

Acknowledgments

Thanks for support to the Unit of Structural Biology (IBMB-CSIC), to the Xaloc beamline at ALBA and to the Crystallography Platform at the Barcelona Science Park (PCB). We thank the staff of the EMBL beamline P14 (PETRA III, Hamburg, Germany) for beamtime allocation and technical support.

Funding: The Switch Laboratory was supported by the Flanders Institute for Biotechnology (VIB, grant no. C0401 to FR and JS) and the Fund for Scientific Research Flanders (FWO; SBO project grant S000722N to FR). Savvas N. Savvides's lab was supported by the Flanders Institute for Biotechnology (VIB, grant no. C0101 to SS). D.V acknowledges financial support from MICINN (Spain) through the Juan de la Cierva-Formación program (JDC2022-048697-I).

Author contributions: Designed the research: RvdK, JS, FR, LSP, ZZ, MD, SNS. Contributed code and ideas: RvdK, JDB, DC, LSP, JS, FR, ZZ, GO. Performed the crystallography experiments: IM and DV. Performed the NMR experiments: ANV. Performed the affinity experiments: TG, KM, CC, ZZ. Performed protein purifications: IM, TG, ZZ, KM. Made visualizations: RvdK, ZZ, IM, ANV. Acquired funding: RvdK, JS, FR, LSP, SNS, MD. Offered supervision throughout the project: RvdK, LSP, JS, FR, MD, SNS. Wrote the manuscript: RvdK, ZZ. Read and contributed to the manuscript: RvdK, ZZ, IM, DV, TG, KM, JDB, DC, GO, CC, ANV, SNS, MD, JS, LSP, FR
Competing interests: RvdK, JS, FR, LSP, JDB, DC. are co-inventors on E.U. provisional patent number EP 24170283.6 which covers the computational antibody design pipeline described here.

Data and materials availability: Crystallographic coordinates and final structure factors have been deposited in the Protein Data Bank (PDB) with access codes: 9EZU (hVSIG4-VHH_h1), 9EZV (hVSIG4-VHH_h2), 9EZW (hVSIG4-VHH_h3), 9EZH (hVSIG4-VHH_h4) and 9EZI (hVSIG4-VHH_h5). The assigned chemical shift lists were deposited in Biological Magnetic Resonance Data Bank (BMRB) entries 52361 (VHH_WT) and 52360 (VHH_h4).

Figures

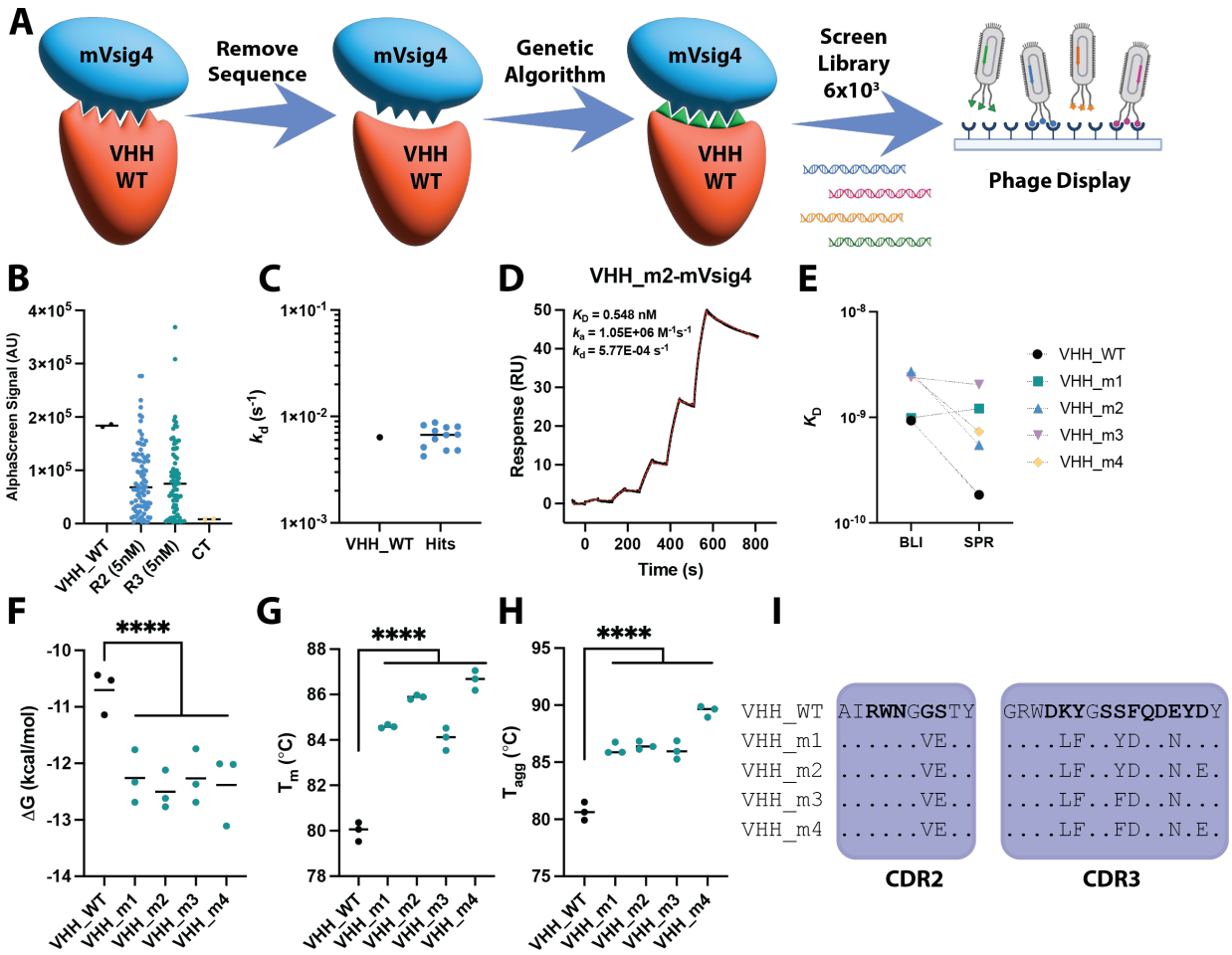

Fig. 1. Library design, screening, hit selection and validation of VHH's designed with EvolveX to bind mouse Vsig4. (**A**) Graphical representation of the EvolveX *in silico* pipeline, where crystal structures of the high affinity complex between mouse Vsig4 (mVsig4) and VHH_WT were used as templates to *in silico* design sequences of CDR2 and CDR3 that should bind mVsig4 with high affinity, while displaying good stability. A small library was subsequently screened using phage display. Icons of DNA strands and phage display were created with BioRender.com. (**B**) Colonies picked after phage display selection were tested for binding to mVsig4 using AlphaScreen. VHH_WT was used as a positive control, colonies picked after two different rounds of selection were screened. (**C**) Off-rates of the top 12 unique sequences based on AlphaScreen signal to mVsig4, determined using BLI. (**D**) Example SPR binding curves of 1 out of 4 hits binding to mVsig4 with low nanomolar affinity. (**E**) Affinity constants of all 4 hits and VHH_WT binding to mVsig4, determined using BLI and SPR. (**F**) ΔG values determined through curve fitting based on data shown in G. (**G**) Melting temperatures (T_m) for 4 hits and VHH_WT based on Intrinsic Tryptophan Fluorescence (ITF) through a temperature ramp. (**H**) Aggregation onset temperatures (T_{agg}) for 4 hits and VHH_WT based on Right Angle Light Scattering (RALS) through a temperature ramp. (**I**) Sequence alignment indicating the differences in sequence compared to VHH_WT. CDR2 and CDR3 are indicated by blue boxes, positions identical to VHH_WT are indicated with a dot (.), positions explored with the EvolveX pipeline are displayed bold on the sequence of VHH_WT.

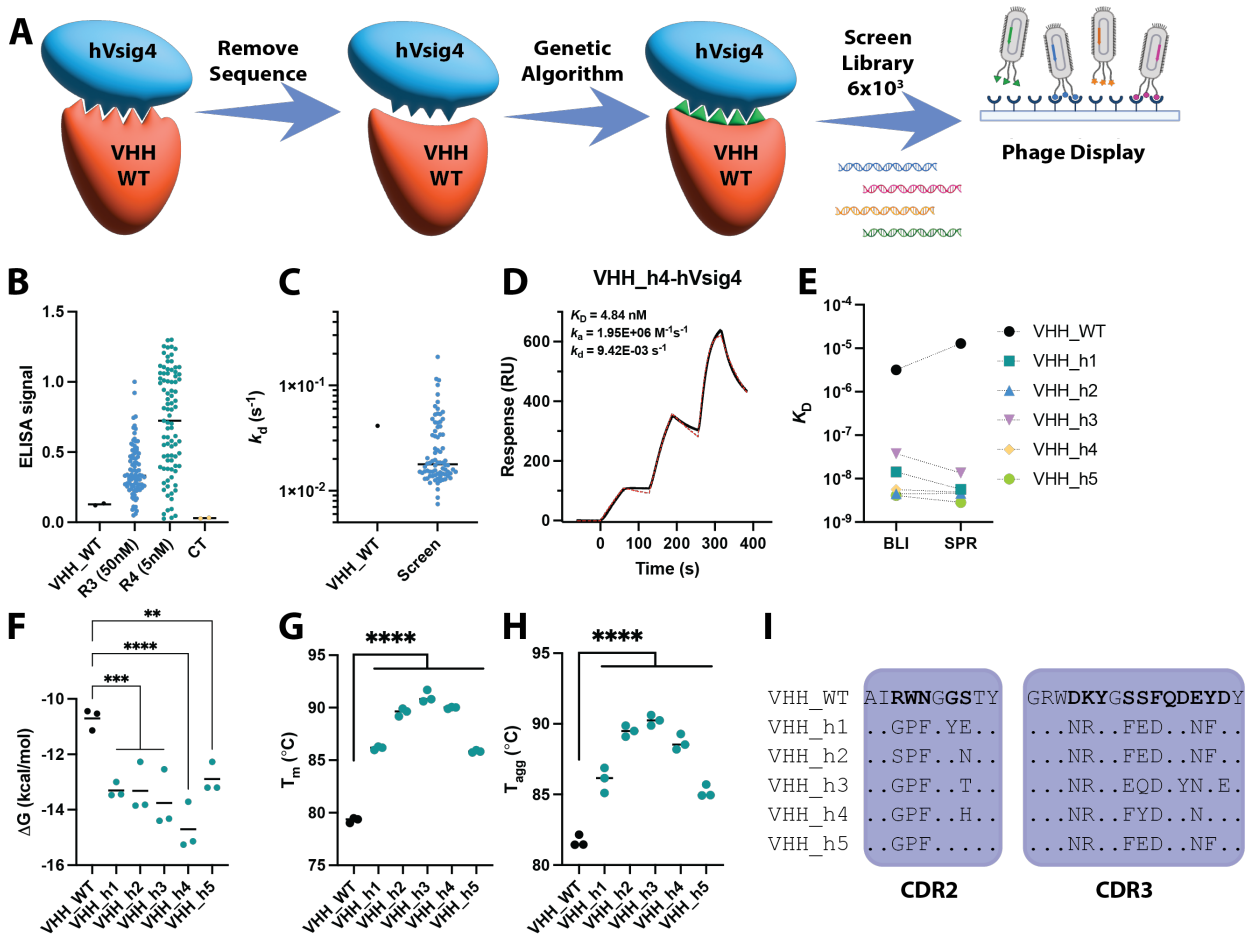

Fig. 2. Library design, screening, hit selection and validation of VHH's designed with EvolveX to bind human Vsig4. (**A**) Graphical representation of the EvolveX *in silico* pipeline, where crystal structures of the low affinity complex between human Vsig4 (hVsig4) and VHH_WT were used as templates to *in silico* design sequences of CDR2 and CDR3 that should bind hVsig4 with high affinity, while displaying good stability. A small library was subsequently screened using phage display. Icons of DNA strands and phage display were created with BioRender.com. (**B**) Colonies picked after phage display selection were tested for binding to hVsig4 using ELISA. VHH_WT was used as a positive control, colonies picked after two different rounds of selection were screened. (**C**) Off-rates of the 82 unique sequences, determined using BLI. (**D**) Example SPR binding curve of 1 out of 5 hits (VHH_h4) binding to hVsig4 with low nanomolar affinity. (**E**) Affinity constants of all 5 hits and VHH_WT binding to hVsig4 determined using BLI and SPR. (**F**) ΔG values determined through curve fitting based on data shown in G. (**G**) Melting temperatures (T_m) for 5 hits and VHH_WT based on Intrinsic Tryptophan Fluorescence (ITF) through a temperature ramp. (**H**) Aggregation onset temperatures (T_{agg}) for 5 hits and VHH_WT based on Right Angle Light Scattering (RALS) through a temperature ramp. (**I**) Sequence alignment indicating the differences in sequence compared to VHH_WT. CDR2 and CDR3 are indicated by blue boxes, positions identical to VHH_WT are indicated with a dot (.), positions explored with the EvolveX pipeline are displayed bold on the sequence of VHH_WT.

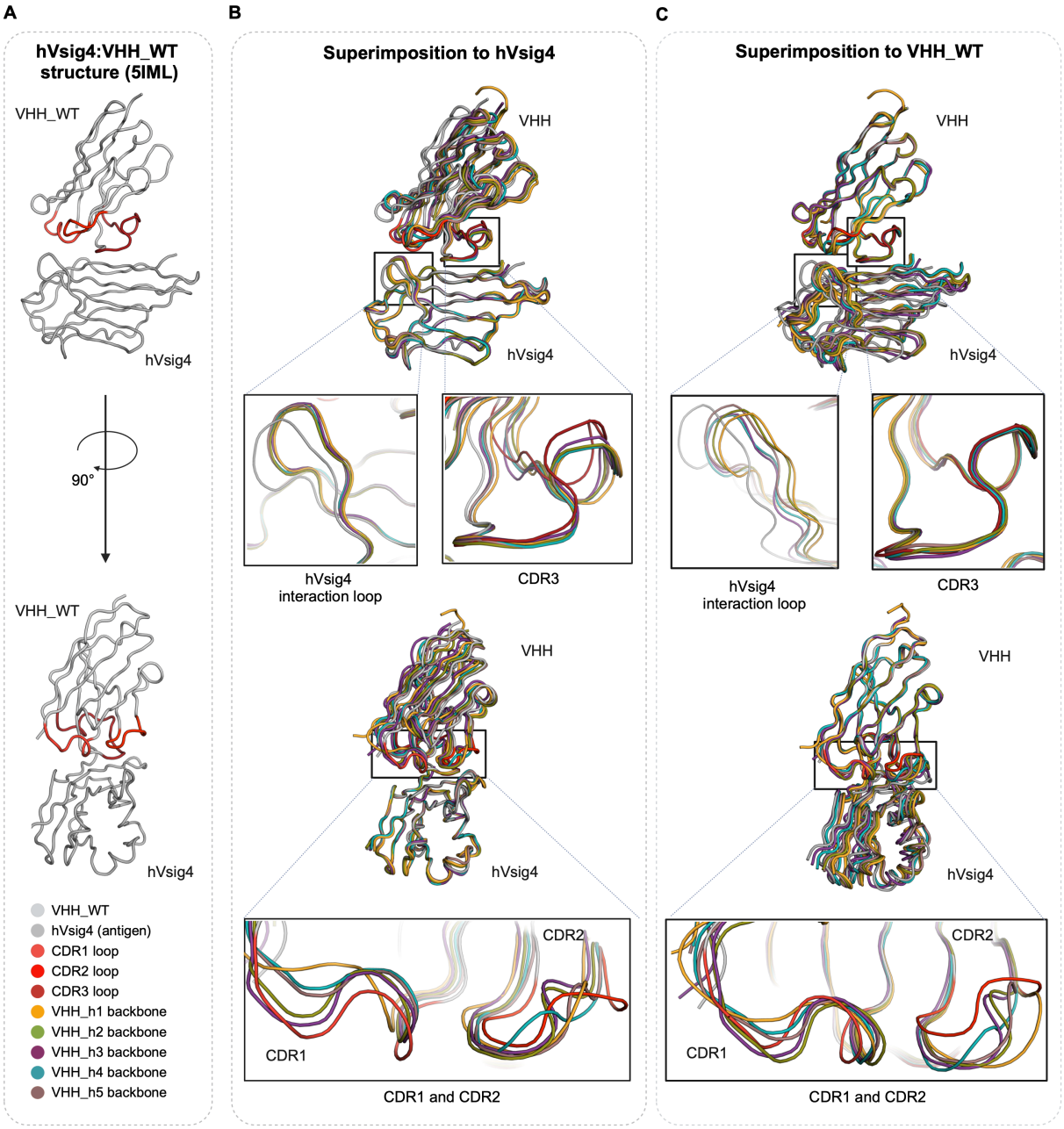

Fig. 3. X-ray crystallography high resolution structures of VHH_h1-h5 show epitope retention and conservation of CDR conformation. (**A**) hVsig4:VHH_WT reference structure (PDB:5IML) represented in 2 views with CDRs shown in red. (**B**) Superimposition of the hVsig4:VHH_WT structure with experimental structures of five in silico designed VHHs in complex with hVsig4 aligned to hVsig4 structure. (**C**) Superimposition of the hVsig4:VHH_WT structure with experimental structures of five in silico designed VHHs in complex with hVsig4 aligned to VHH_WT structure. Superimpositions were generated in Pymol using the align function.

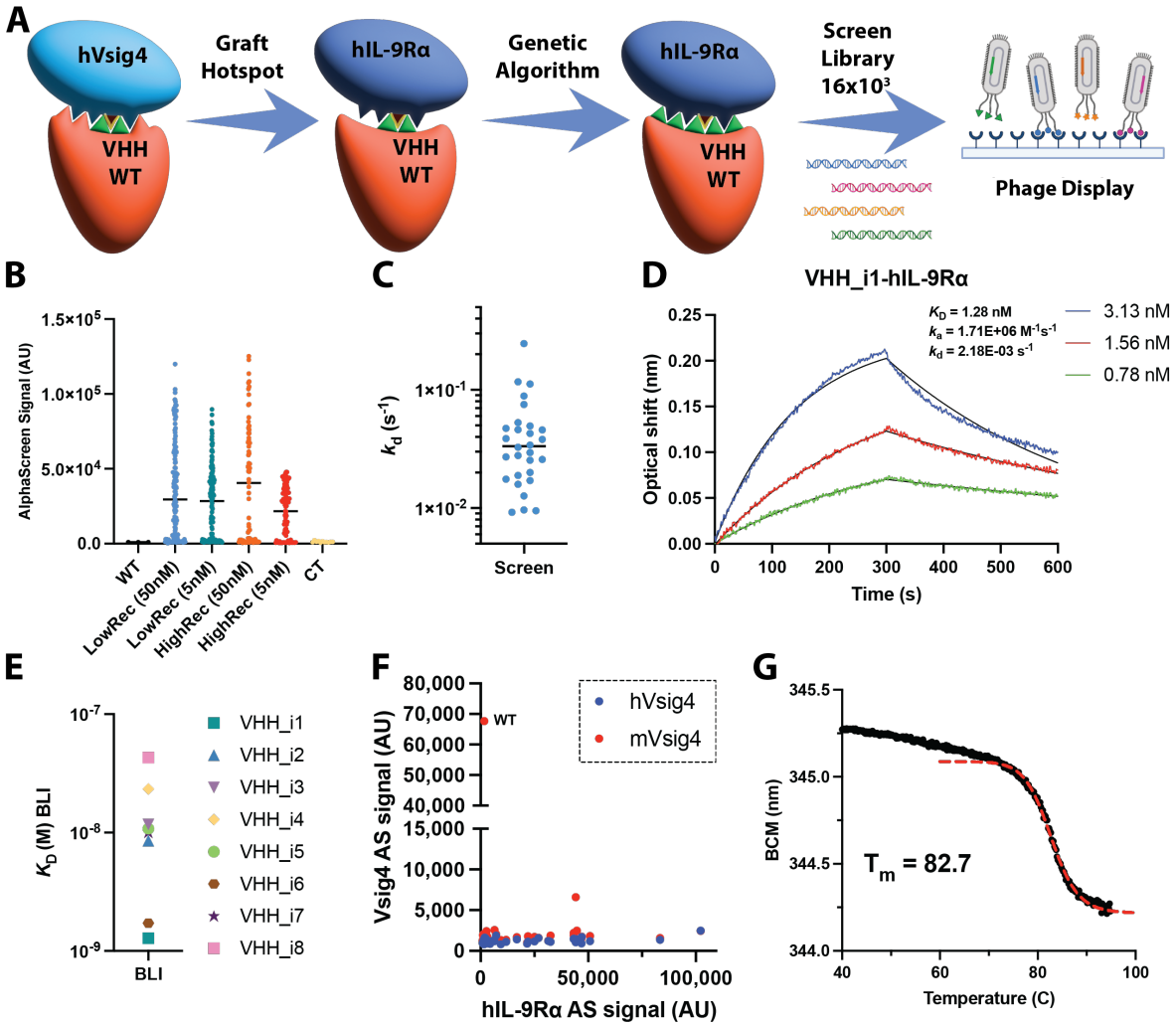

Fig. 4. *De novo in silico* design of single digit nanomolar binding to human interleukin-9 receptor alpha (hIL-9Rα) using hotspot grafting and antibody design. (**A**) Graphical representation of the EvolveX *in silico* pipeline, where crystal structures of the low affinity complex between human Interleukin-9 Receptor alpha (hIL-9Rα) and VHH_WT were used as templates to dock VHH_WT onto an Alphafold model of hIL-9Rα using one hotspot as an anchoring point. Subsequently all three CDRs were *in silico* designed, to create sequences able to bind hIL-9Rα with high affinity, while displaying good stability. A small library was subsequently screened using phage display. Icons of DNA strands and phage display were created with BioRender.com. (**B**) Colonies picked after phage display selection were tested for binding to hIL-9Rα using AlphaScreen. VHH_WT was used as a positive control, colonies picked after two different rounds of selection were screened. (**C**) Off-rates of the 82 unique sequences, determined using BLI. (**D**) Example BLI binding curve of 1 out of 5 hits (VHH_i1) binding to hIL-9Rα with low nanomolar affinity. (**E**) Affinity constants of all 5 hits and VHH_WT binding to hIL-9Rα determined using BLI. (**F**) Hits were tested for binding to mVsig4, hVsig4 and hIL-9Rα using AlphaScreen, confirming specificity. (**G**) Thermal unfolding curve for the highest affinity hit based on Intrinsic Tryptophan Fluorescence (ITF) through a temperature ramp.

Supplementary Materials and Methods

Vsig4 preparation

Mouse recombinant Vsig4 (mVsig4) used in phage selection, screening, and VHH affinity measurement was bought from Sino Biological (50187-M08H-100) and biotinylated with EZ-Link NHS-PEG4-Biotin (Thermo Scientific, A39259) according to the manufacturer instructions. The mVsig4 material used for crystallization (amino acids 20-139, with C-terminal His tags) was cloned into plasmid pVDS101 (a modified version of pHEN6), expressed in TG1 *E. coli* strain, and purified from the periplasmic extract by a Ni-charged column followed by a size exclusion chromatography (SEC) (Superdex 75 16/600 column).

Human recombinant Vsig4 (hVsig4) used in phage selection, screening, and VHH affinity measurement (amino acids 20-137, with C-terminal Avitag and His tags) was cloned into pVDS101 plasmid and expressed in AVB101 *E. coli* strain (AVIDITY) to allow *in vivo* biotinylation, following the suggested protocol. Then the protein was extracted from periplasm and purified by Ni-NTA chromatography. The hVsig4 protein used in crystallization (amino acids 20-137, with C-terminal His tags), was cloned into pLTDA104 plasmid (also a modified version of pHEN6), expressed in TG1 *E. coli* strain and purified following the same procedures with mVsig4.

Production of recombinant hIL-9Rα

Production of recombinant hIL-9Rα was done as previously described by de Vos et al (*27*). In brief, hIL9Rα (NP_002177.2, residues 40-261) with a N-terminal His-tag followed by a thrombin cleavage site was expressed *in E. coli* BL21(DE3) using pET15b-hIL-9Rα expression construct. Following refolding based on an in-house protocol (*30*), hIL-9Rα was purified by immobilized metal affinity chromatography (IMAC) followed by SEC. The N-terminal His-tag was removed using thrombin (Merck). Undigested protein was removed by IMAC and the cleaved protein was purified via SEC using HBS pH 7.4 buffer.

In vitro biotinylation of recombinant hIL-9Rα

In vitro biotinylation of hIL-9Rα was done using EZ-LinkTM Sulfo-NHS-LC-Biotinylation Kit (Thermo Scientific™) following manufacturers protocol. The excess biotin was removed by a desalting step using the HiPrep 26/10 Desalting column (Cytiva). The biotinylated protein was aliquoted and flashfrozen in liquid nitrogen.

Cloning of the synthetic Vsig4 CDR23 VHH library

The oligo pool containing 12,405 sequences (12,405 CDR pairs, 3200 unique CDR2s, 9884 unique CDR3s), encoding for the region from CDR2 to CDR3 of the VHHs, flanked by two restriction sites (BpiI and Eco91I) was ordered at Twist Biosciences. The oligo pool was amplified with a KAPA HiFi HotStart ReadyMix PCR Kit (Roche, KK2602). The amplified product was then restriction digested and ligated into the phagemid vector pP002ph008 (a modified version of pMECS, which encodes for the non-library encoded parts of VHH_WT, followed by 3xFlag/6xHis tag at the C-terminus of the VHH insertion site) with T4 DNA ligase (Thermo Scientific, EL0011) at 16°C overnight. The purified ligation sample was transformed into the TG1 electrocompetent cells (Lucigen, 60502-2). The resulting library had a size of >10^7 CFU and a high insertion rate (> 90 %). At last, the phage

library was produced with the infection of M13KO7 helper phage (Thermo Fisher Scientific, 18311019) according to the protocol published by Pardon et al(*31*).

Cloning of the synthetic hIL9R VHH library

The oligo pool containing 16,477 sequences (16,477 CDR pairs, 738 unique CDR1s, 862 unique CDR2s and 11,298 CDR3s) was ordered at Twist Biosciences and amplified similarly as above. To clone the low recombined phage library (LowRec), the full-length oligo pool was cloned into pP002ph012 (also a modified version of pMECS, which encodes for the non-library encoded parts of VHH_WT, followed by 3xFlag/6xHis tag at the C-terminus of the VHH insertion site) by conventional restriction digest and ligation protocols. To clone the high recombined phage library (HighRec), all three CDR regions were shuffled by golden gate assembly into phagemid vector pP002ph012. Both libraries got a good size and insertion rate, and the phage libraries were produced following the same procedure as above.

Phage library selection

The VHH displaying phage library was selected against multiple rounds of mVsig4, hVsig4 or hIL9R according to the standard protocol (*31*) (fig S1 and fig S22). Briefly, $2x10^{11}$ CFU of phages, biotinylated antigens, and streptavidin magnetic beads (Thermo Scientific, 88817) were firstly blocked at PBS buffer with 2% of milk for at least 0.5h at room temperature. Then the blocked phages and antigens were co-incubated for 2h at room temperature to allow the binding of VHH-displaying phages with the targets. Non-binding phages were discarded with 5 consecutive washing steps with PBS/2% milk, whereas bound phages were captured by the streptavidin beads and eluted by trypsin. The eluted phages were rescued with the exponentially grown TG1 cells for the next round of selection. In the end, the output phage libraries from desired rounds of selection were sub-cloned into the vector pLTDA118 (a modified pHEN6 vector with C-terminal 3xFlag/6xHis tag) and transformed into TG1 cells. Single colonies were randomly picked to grow in the 96-well deep-well plate for the preparation of periplasmic extracts, and Sanger sequenced as previously described (*32*).

AlphaScreen

AlphaScreen FLAG (M2) detection kit (PerkinElmer, 6760613M) was used for the initial screening of the mVsig4 hits and hIL9R hits. In short, in a 384-well Optiplate (PerkinElmer, 6007290), 5µL of diluted biotinylated mVsig4 or hIL9R, 5µL of diluted periplasmic extracts in a 96-well plate from different clones, and 10µL of anti-FLAG conjugated acceptor beads (50µg/ml) were incubated together for 1h at room temperature in the dark. Then 5µL of streptavidin donor beads (100µg/mL) was added and incubated in the dark for 25-30 minutes. The signals were read (excitation 680nm; emission: 520-620nm) using the EnVision multilabel plate readers (PerkinElmer).

ELISA screen

Human Vsig4 hits were first screened in an ELISA assay. In brief, 100µL of biotinylated hVsig4 (2µg/mL) was coated in the ELISA plate in advance. The plates were blocked with PBS/1% BSA for 2h at room temperature. Subsequently, 100µL of periplasmic extracts were added per well, and incubated for 1.5h at room temperature. Then 100µL/well of anti-FLAG-HRP antibody (Sigma-

Aldrich A8592) (1:2500 dilution) was added and incubated for 1 more hour. At last, TMB solution (50µL/well) was used to detect and after 1-5 minutes, 50µL/well of H_2SO_4 was added to stop the reaction. The plates were then read at 450nm of wavelength in a plate reader.

Biolayer interferometry (BLI) off-rate assay

The clones with unique sequences and significant AlphaScreen or ELISA signal (signal/noise, S/N > 3) were further selected, re-arrayed in a 96-well plate, and screened by a biolayer interferometry (BLI) off-rate assay on Octet RED96 (Sartorius). Ni-NTA biosensors (Sartorius, 18-5101) were first used to assess the expression of different clones. After equilibration of the biosensors for at least 10 minutes in 1x Sartorius/Octet kinetic buffer and an extra 120 seconds for the baseline, the biosensors were dipped into 10x diluted periplasmatic extracts for 300 seconds, followed by 300 seconds of dissociation in 1x kinetic buffer. Afterward, streptavidin (SA) biosensors (Sartorius, 18-5019) were used to measure the off rate of different clones. With the same pre-wet procedure and the baseline setting, biotinylated Vsig4 or IL-9Rα material was first loaded on the biosensors, after which, the tips were sequentially submerged in baseline wells, association wells with diluted periplasm samples (300s), and finally into the dissociation wells (300s). Data was processed on the Octet RED analysis software.

VHH expression and purification

VHH candidates used for initial affinity measurement were in the vector pLTDA118 (a modified pHEN6 vector with C-terminal 3xFlag/6xHis tag) and expressed in the TG1 cells following the standard protocol (*31*). The purification of these VHHs was done by either the Ni-NTA chromatography or the AmMag™ SA Plus System (Genscript, L01013) with Ni magnetic beads (Genscript, L00776). VHHs used in stability study and crystallization were cloned into the vector pLTDA104 (a modified pHEN6 vector with C-terminal 6xHis tag) and expressed in the TG1 cells following the same procedure. These VHHs were then purified by a Ni-charged column followed by size exclusion chromatography (SEC).

Biolayer interferometry (BLI) affinity measurement

Purified VHHs were used to determine the affinity with mVsig4 and hVsig4 on Octet RED96 (Sartorius). Briefly, streptavidin (SA) biosensors (Sartorius, 18-5019) were first equilibrated for at least 10 minutes in 1x Sartorius/Octet kinetic buffer. Subsequently, the tips were dipped into the biotinylated Vsig4 (3-5µg/mL) target for 30-60 seconds. Afterward, the tips were sequentially submerged in the 1x kinetic buffer for the baseline (120s), VHH dilution samples for the association (300s), and in the end back to the 1x kinetic buffer for the dissociation (300s). Fitting and binding kinetics determination was performed with a 1:1 model interaction on the Octet RED analysis software.

Surface plasmon resonance (SPR) affinity measurement

Binding kinetics and affinity of various VHHs for the human and murine Vsig4 were evaluated by surface plasmon resonance on a BIAcore T200 instrument (Cytiva) with a running buffer composed of 10mM HEPES, 150mM NaCl & 0.005% Tween 20. The assay format involved ligand capture on a Sensor S Sensor Chip SA chip. Briefly, the biotinylated ligands were immobilized by non-covalent capture (binding to streptavidin) following the instructions provided with the Cytiva

chip. mVSIG4 was captured on flow cell 2, and hVSIG4 was captured on flow cell 3, leaving flow cell 1 as a subtractive reference. The capture level of the mVsig4 was targeted between 100 and 200 resonance units, and the hVsig4 was targeted between 1200 and 1300 resonance units. A serial dilution of the VHHs was flowed over the immobilized Vsig4 (50µL/min for 1 minute) and allowed to dissociate for 4 minutes. The capture surface was regenerated with a 60-s injection of 3 M MgCl2 (50 µL/min for 1 min). A 3-fold concentration dilution series of each VHH variant ranging was used to analyze binding to mVsig4. For the VHH_WT, VHH_m1-VHH_m4 the concentration series ranged from 0.25nM to 20nM. For the VHH_h1-VHH_h5 the concentration dilution series ranged from 6.2nM to 500nM. A 3-fold concentration dilution series of each VHH variant ranging was used to analyze binding to hVsig4. For the WT and VHH_m1, the concentration dilution series ranged from 3.7nM to 300nM. For VHH_h1-VHH_h5 and VHH_m4 the concentration dilution series ranged from 0.25nM 20nM. For the VHH_m2 and VHH_m3, the concentration dilution series ranged from 2.1nM to 167nM. All sensograms were analyzed using a 1:1 Langmuir binding model with software supplied by the manufacturer to calculate the kinetics and binding constants.

Thermal stability measurement

The temperature at which 1.0 mg/mL VHHs unfold (T_m, unfolding temperature) and aggregate (T_{agg}, aggregation onset temperature) using an UNcle device (Unchained Labs, CA, USA). More specifically, the T_m and T_{agg} were determined simultaneously via intrinsic fluorescence (ITF) and static light scattering (SLS) measurements, respectively, during gradual heating from 15 to 95°C at 0.3°C/min. The excitation wavelength of 280 nm was used for both measurements, with the emission wavelength ranging from 250 to 720 nm for the intrinsic fluorescence and corresponding to 266 nm for the SLS. The intrinsic fluorescence values between 320 and 370 were used to calculate the barycentric mean values (BCMs), resulting in a smooth curve. Curve fitting with R-studio was used to calculate the T_m value corresponding to the inflection point of the sigmoid curve. The T_{agg} value was determined using manually set thresholds, to allow for proper comparison between variants, ignoring baseline noise. All samples were measured at least in triplicate.

Chemical stability measurement

Chemical denaturation was performed using both Urea (0-9.2M) and Guanidine Hydrochloride (GdnHCl, 0-5.5M) using a gradient of 24 steps. Pipetting the different steps was done using a robot (Opentrons OT-2) from a protein stock solution of 1 mg/mL in PBS with a final concentration of 0.04 mg/mL and freshly prepared denaturant stock solution of 10M Urea or 6M GdnHCl. All stock solutions were filtered using 0.22 µM filter. After pipetting, plates were spun down in a centrifuge at 1000g for 2 minutes. The plates were incubated for 2 hours at 25ºC with a lid to avoid evaporation of the sample. Samples were measured using the standard protocol on the SUPR-CM (ProteinStable).

Crystallization of the VHH:hVsig4 complexes

For VHH_h1, VHH_h2 and VHH_h3 complexes with hVsig4, 1.2 molar excess of VHH was added to hVsig4, incubated for 15 minutes at room temperature and purified by SEC on a Superdex 75 Increase 10/300 (Cytiva) column using HBS pH 7.4 buffer. Fractions containing the complex were

pooled and concentrated to 4 - 6 mg/ml. Crystallization screens were set up using a Mosquito liquid handling robot (TTP Labtech) in sitting-drop format using 100 nl of protein mixed with 100 nl of mother liquor in SwissSci 96-well triple drop plates incubated at 287 or 294 K. VHH_h2:hVsig4 complex hit was obtained by micro-seeding using crystal seeds of VHH_h1:hVsig4 complex grown in condition 0,17M ammonium sulfate, 15% glycerol, 30,5% PEG 4000. Seed stock was prepared by crushing the crystals with a loop in original mother liquor drop. Crystal seeds were added using a cat whisker to drops containing 100 nl of protein mixed with 100 nl of mother liquor in multiple conditions. Plate was incubated at 287K. Best diffracting crystal of this complex was obtained in 0,1M Na-citrate pH 5,6, 20% 2-propanol and 21% PEG 4000. Crystals were cryoprotected in mother liquor containing glycerol or ethylene glycol prior to being cryocooled in liquid nitrogen. Diffraction data was collected at 100 K at the P13 microfocus beamline at PETRA III (Hamburg, Germany).

For VHH_h4 and VHH_h5 complexes with hVsig4, VHH and hVsig4 were mixed in a 1:1 molar ratio respectively, incubated for 40 minutes at room temperature and purified by size exclusion chromatography (SEC) on a Superdex 75 Increase 10/300 (Cytiva) column using 20mM Tris pH 7.5, 5% Glycerol and 150mM NaCl buffer. Fractions containing the complex were pooled and concentrated to 3.5-4.5 mg/ml. The crystallization screens were set up using the hanging drop vapor-diffusion technique by mixing 1 µl of protein solution with 1 µl of mother liquor. For this purpose crystallization conditions consisting of 0.1M Bis-Tris pH 6.0-6.5 and 25-30% PEG 3350 were used, based on the previously reported conditions that yielded crystals of native VHH_WT:hVsig4 complexes (*23*). Plates were incubated at 293K. Obtained crystals were cryoprotected in mother liquor containing 15% glycerol prior to being cryocooled in liquid nitrogen. Diffraction data was collected at 100 K at the Xaloc beamline at ALBA (Barcelona, Spain). Detailed crystallography setup and data collection statistics are summarized in table S7.

Determination of crystallographic structures of the VHH:hVsig4 complexes

Datasets for complexes of VHH_h1, VHH_h2 and VHH_h3 were integrated and scaled using XDS (*33*) and AIMLESS and the data quality was analyses by Phenix Xtriage and datasets for complexes of VHH_h4 and VHH_h5 with hVsig4 were processed with autoPROC (*34*) and

Initial phases for the VHH:hVsg4 complexes were obtained by maximum-likelihood molecular replacement with Phaser (*35*) using the coordinates of native structures of hVsig4 and VHH (PDB ID 5IML) as a search model. A model for each of the VHH variants was manually rebuilt in Coot (*36*) and the refinement of coordinates and atomic displacement parameters for all the structures was performed in Refmac (*37*) and Phenix refine (*38*). Model and map validation tools in Coot and the PHENIX suite were used throughout the workflow to guide improvement and validate the quality of crystallographic models. Refinement statistics are summarized in table S7.

NMR spectroscopy

The NMR samples contained 0.8-1 mM [^{13}C,^{15}N] or ^{15}N VHH in 20 mM sodium phosphate 50 mM NaCl pH 6.5, 0.02% NaN_3, and 10 % D_2O for the lock. All NMR spectra were acquired at 313 K on a Bruker Avance III HD 800 MHz spectrometer, equipped with a triple-resonance TCI cryoprobe for enhanced sensitivity. Three-dimensional experiments were acquired with a non-uniform sampling (25-50%) as implemented in TopSpin 3.7 (Bruker). The NMR data were processed in

TopSpin 3.7 (Bruker) or MddNMR (*39*) and NMRPipe (*40*), and analyzed in CCPNMR (*41*). Assignments of protein backbone resonances were obtained from [^{13}C,^{15}N]-labelled samples of C-terminally triFlag- and His-tagged VHH_WT and VHH_h4 by establishing intra- and inter-residue connectivities in 3D HNCACB, HN(CO)CACB, HNCO, HN(CA)CO, and HBHA(CO)HN spectra at the corresponding peak frequencies in the 2D [^{1}H,^{15}N]-HSQC spectrum. The assignments were subsequently transferred to [^{1}H,^{15}N]-HSQC spectra of ^{15}N-labelled C-terminally His-tagged VHH_WT and VHH_h4 constructs and verified by 3D ^{15}N-NOESY-HSQC (mixing time 120 ms). The assigned chemical shift lists were deposited in Biological Magnetic Resonance Data Bank (BMRB) entries 52361 (VHH_WT) and 52360 (VHH_h4). The VHH secondary structure (fig S16 and fig S18) was predicted from the backbone chemical shifts using the CSI function and the DANGLE module (*42*) in CCPNMR (*41*) or the web-based RCI (*43*).

Relaxation measurements were performed on ^{15}N-labelled samples of C-terminally His-tagged VHH_WT and VHH_h4. Longitudinal (R_1) and transverse (R_2) relaxation rates were obtained from [^{1}H,^{15}N] HSQC-based pseudo-3D spectra with interscan delays of 2.5 s. The inversion recovery experiment (R_1) had relaxation delays of 10, 100, 1000, 400, 600, 800, 500, 1200, 200, 50, 100, 300, 900 ms (in this order), while Carr-Purcell-Meiboom-Gill (CMPG) measurments (R_2) employed relaxation delays of 17, 68, 136, 170, 85, 34, 51, 34, 119, 153, 102 ms (in this order). Steady-state, heteronuclear {^{1}H}-^{15}N NOEs were measured in an interleaved experiment with and without ^{1}H saturation and the relaxation delay of 6 s and performed in duplicate to estimate the experimental errors. For each analysed [^{1}H,^{15}N]-HSQC peak, the R_1 and R_2 values were obtained from exponential decays of signal intensities in CCPNMR (*41*), while {^{1}H}-^{15}N NOEs were determined as ratios of peak intensities in the spectra with and without ^{1}H saturation. Relaxation analysis was performed with Modelfree v 4.20 (*44*) using FastModelfree setup (*45*). Initial estimates of the diffusion tensor parameters were obtained with quadric_diffusion (*46*) from the experimental R_2/R_1 data that excluded the residues with high R_2 values ($R_2 \geq \langle R_2 \rangle + \sigma_{R2}$) as likely exhibiting significant internal motions. The hydrodynamic parameters and predicted R_2/R_1 ratios were calculated with HYDRONMR (*47*) from the atomic coordinates of VHH_WT taken from the X-ray structure of its complex with Vsgi4 (5IMM).

Supplementary Figures

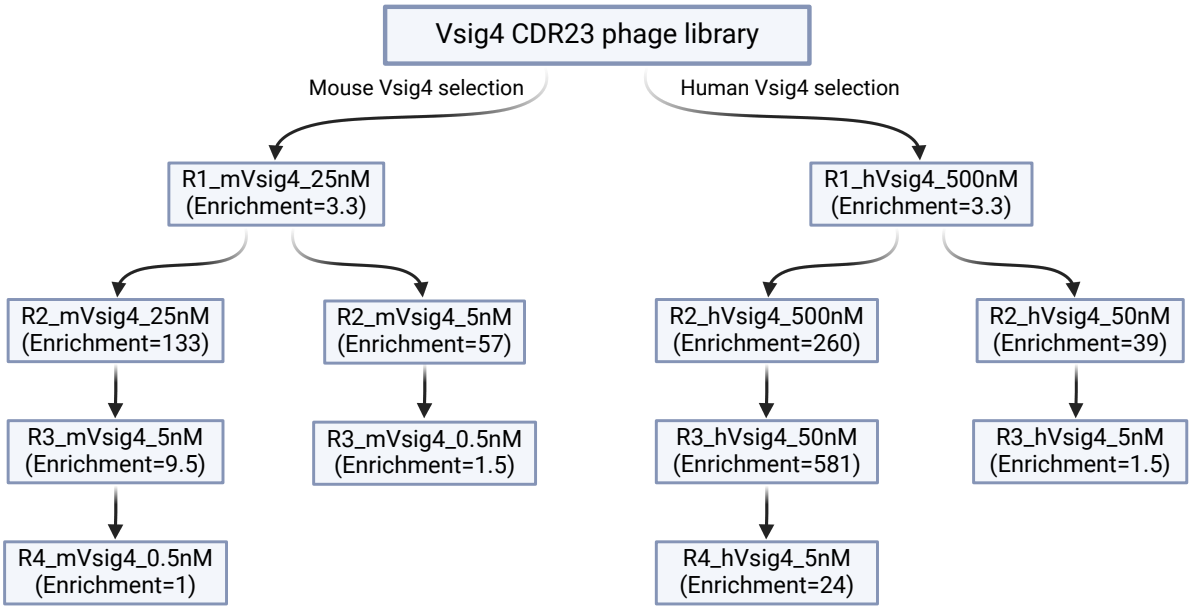

Fig. S1. Phage library selection rounds for the combined Vsig4 CDR23 library. Graphical designs were created with BioRender.com.

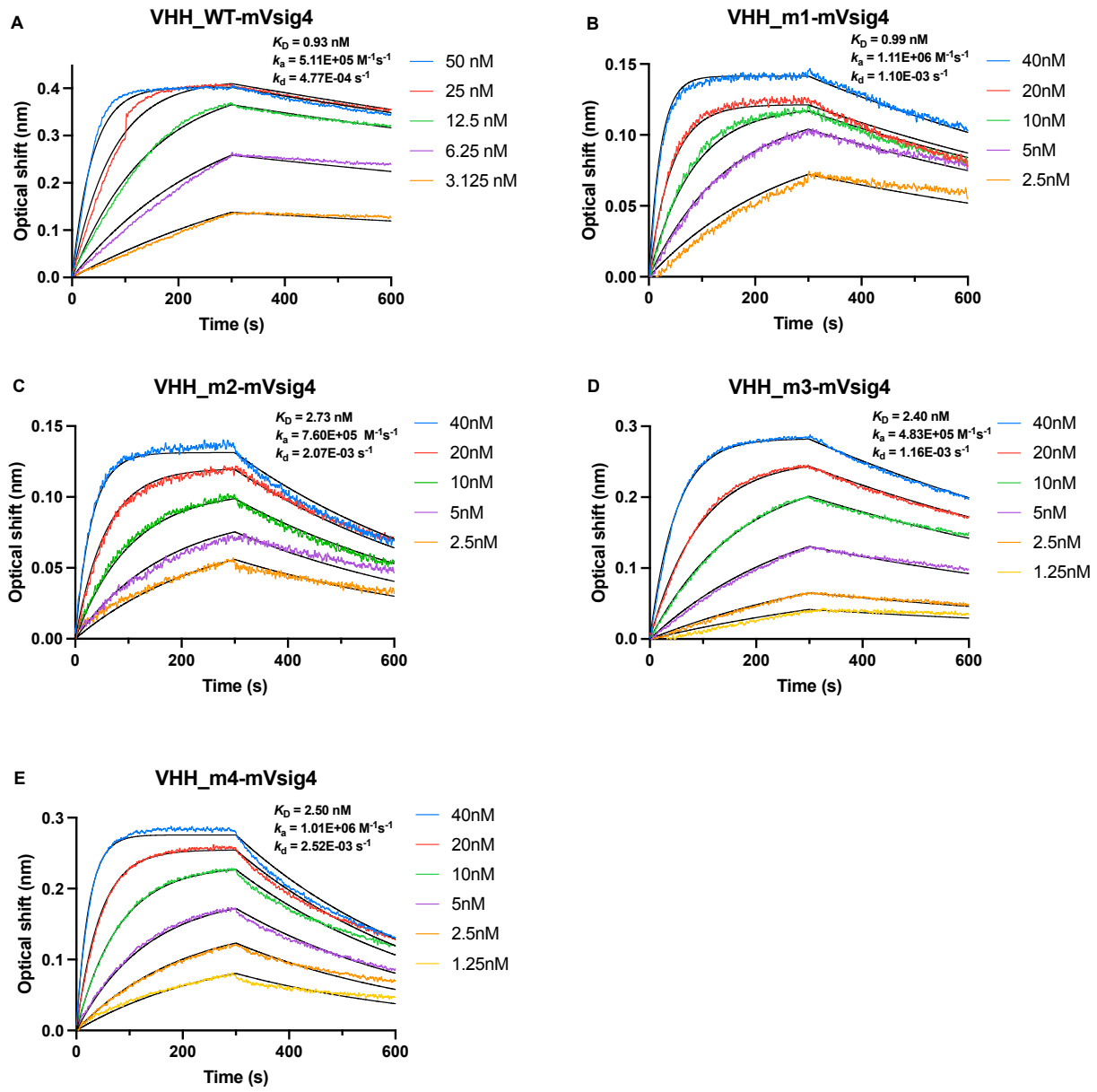

Fig. S2. The binding curves (colored) of VHH_WT, VHH_m1-VHH_m4 against mVsig4 (BLI) with fitting curves (black).

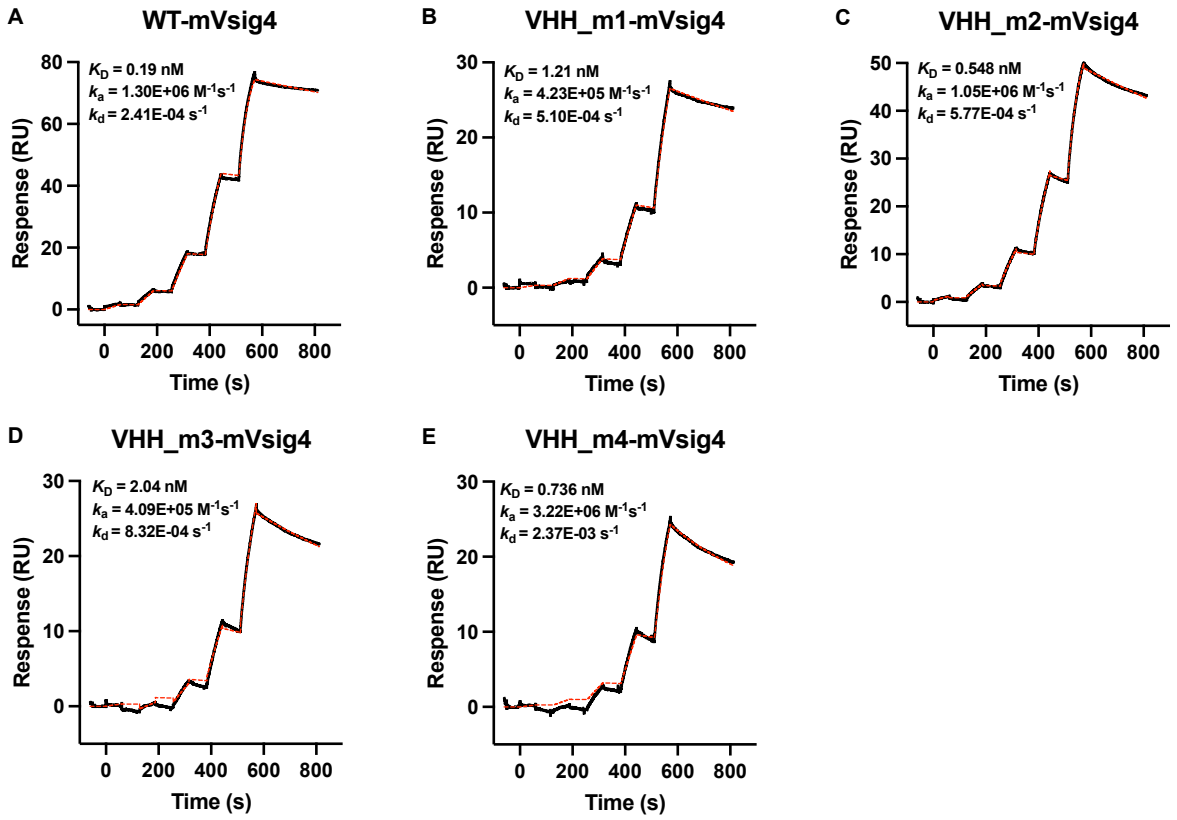

Fig. S3. The binding curves (black) of VHH_WT, VHH_m1-VHH_m4 against mVsig4 (SPR) with fitting curves (red).

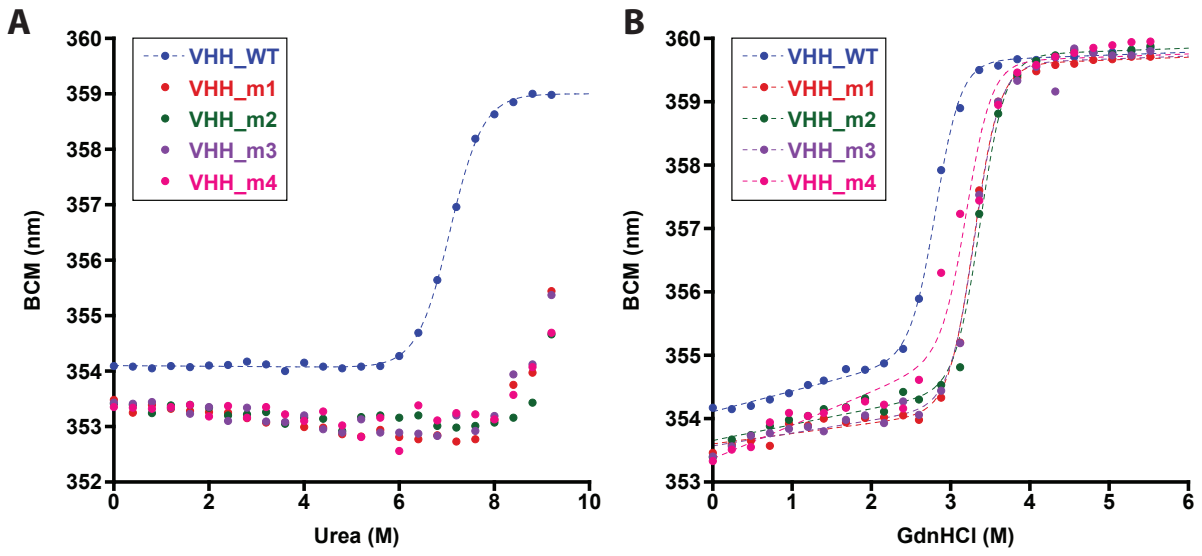

Fig. S4. Representative chemical denaturation curves of VHH_WT, VHH_m1-m4. (A) Urea denaturation. **(B)** GndHCl denaturation. Fits were done using Kaleidagraph. Average ΔG is listed in table S3.

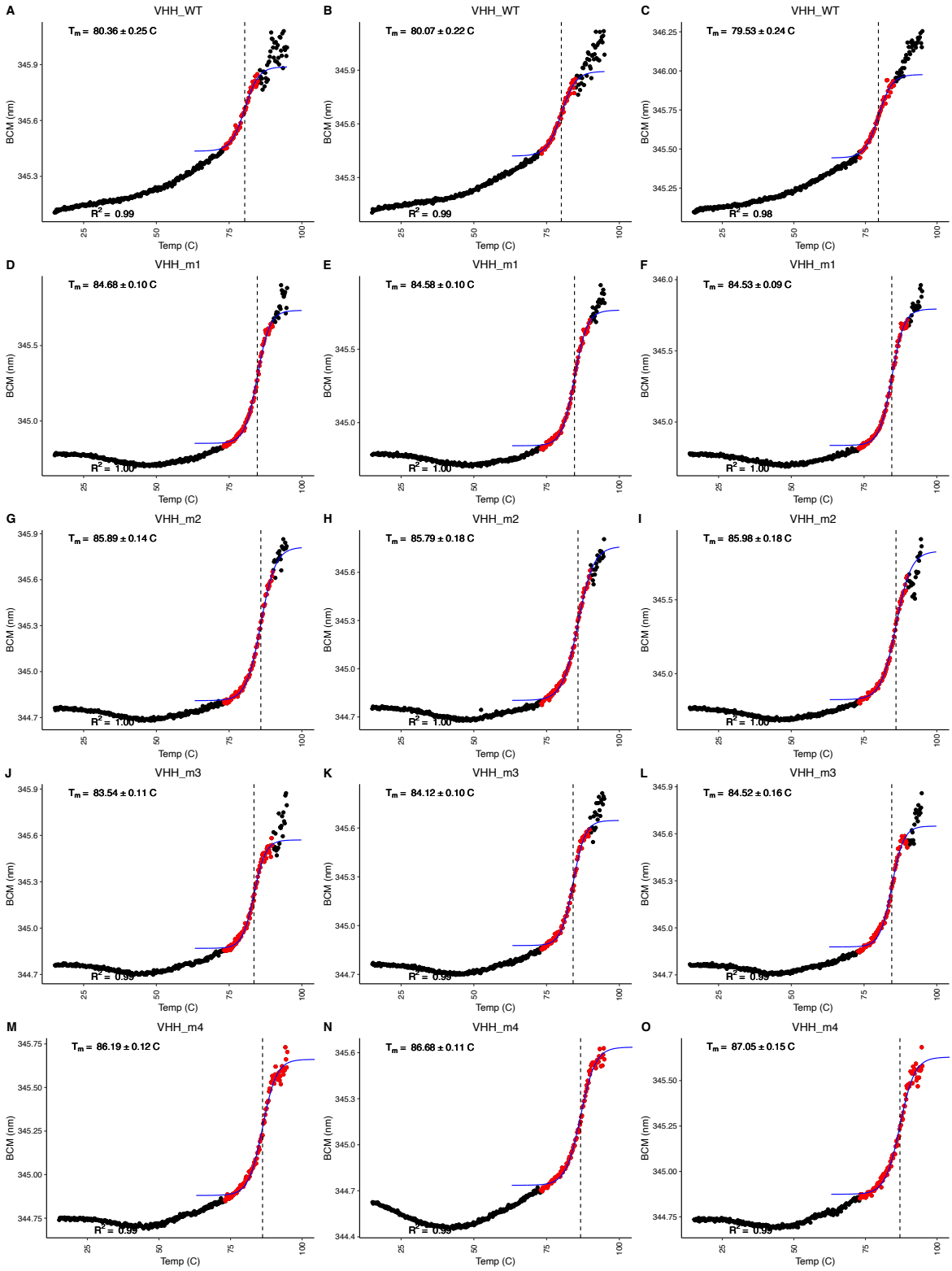

Fig. S5. T_m determination based on Barycentric Mean calculation from Intrinsic Tryptophan Fluorescence (ITF) during a temperature ramp for VHH_WT, VHH_m1-VHH_m4.

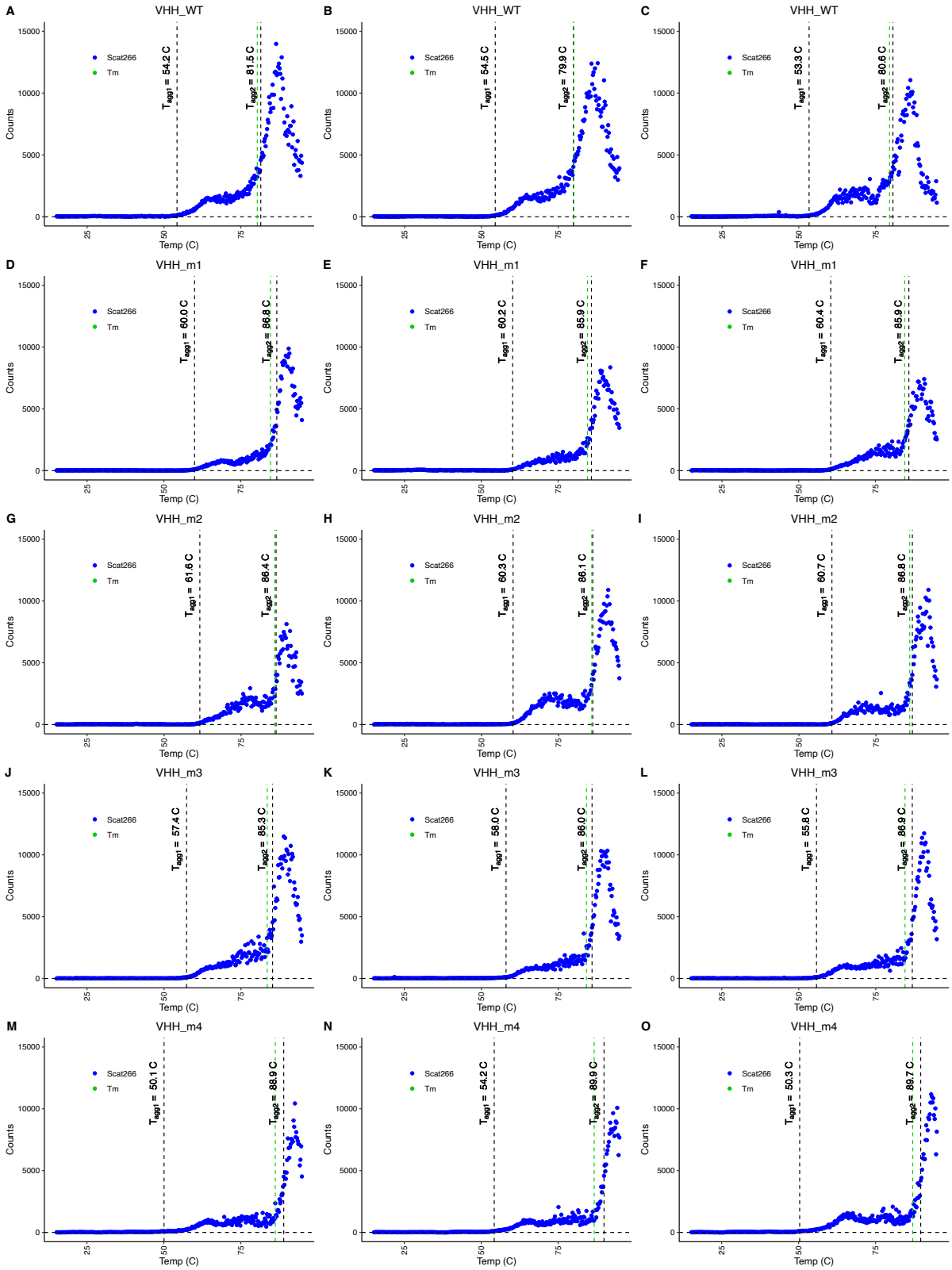

Fig. S6. T_{agg} determination based on Scatting at 266 nm from Right Angle Light Scattering (RALS) during a temperature ramp for VHH_WT, VHH_m1-VHH_m4.

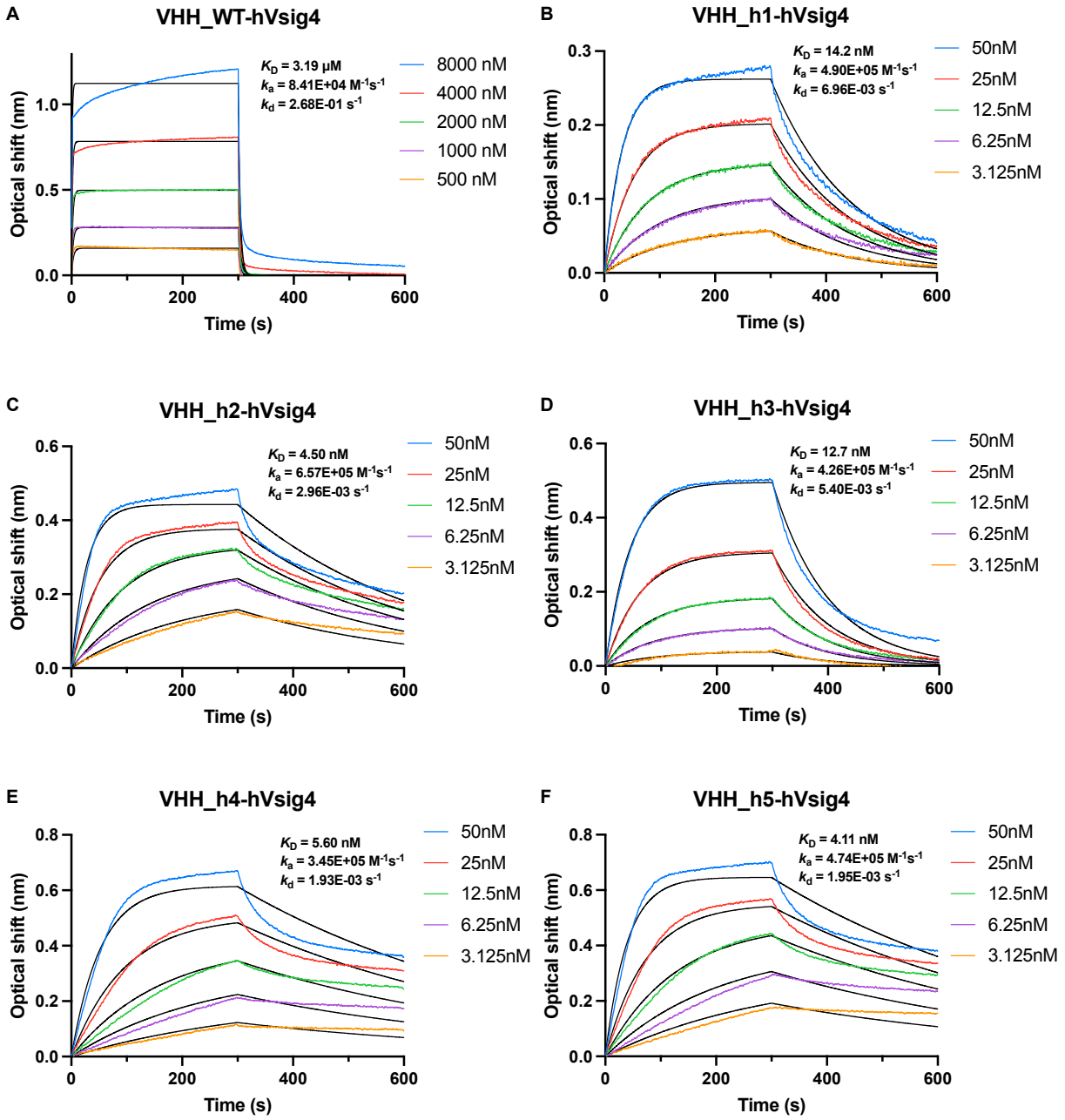

Fig. S7. The binding curves (colored) of VHH_WT, VHH_h1-VHH_h5 against hVsig4 (BLI) with fitting curves (black).

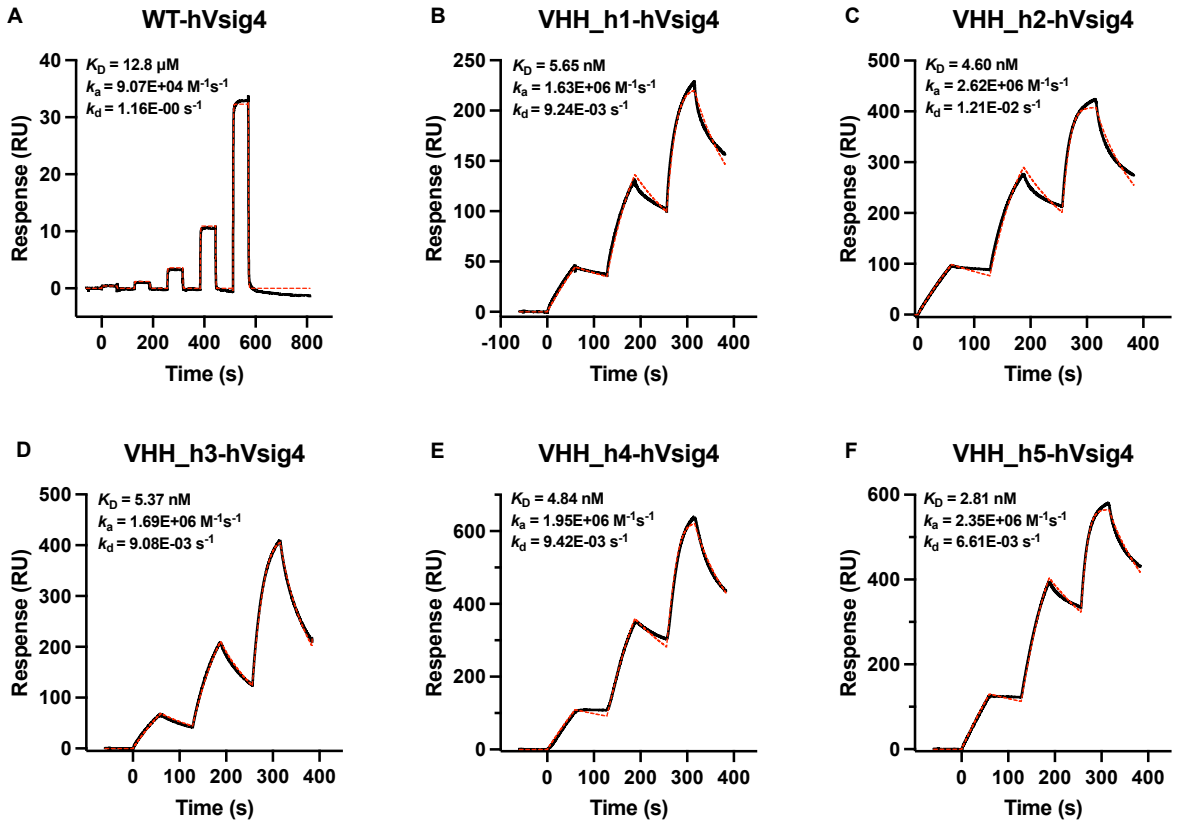

Fig. S8. The binding curves (black) of VHH_WT, VHH_h1-VHH_h5 against hVsig4 (SPR) with fitting curves (red).

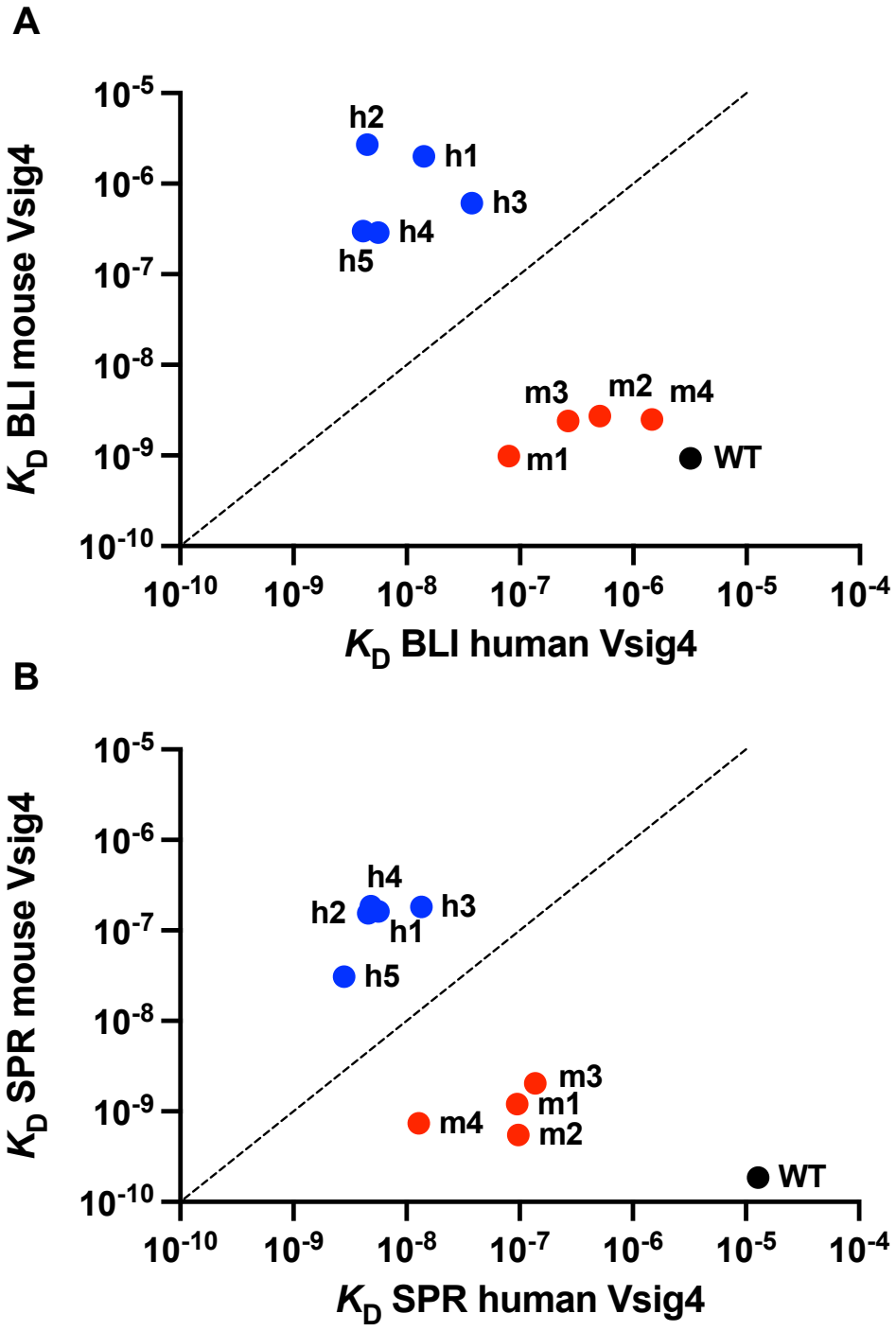

Fig. S9. Binding of VHH_WT, VHH_m and VHH_h hits to mVsig4 and hVsig4. (A) Affinity constants measured by BLI of all Vsig4 hits to both mVsig4 and hVsig4. **(B)** Affinity constants measured by SPR of all Vsig4 hits to both mVsig4 and hVsig4.

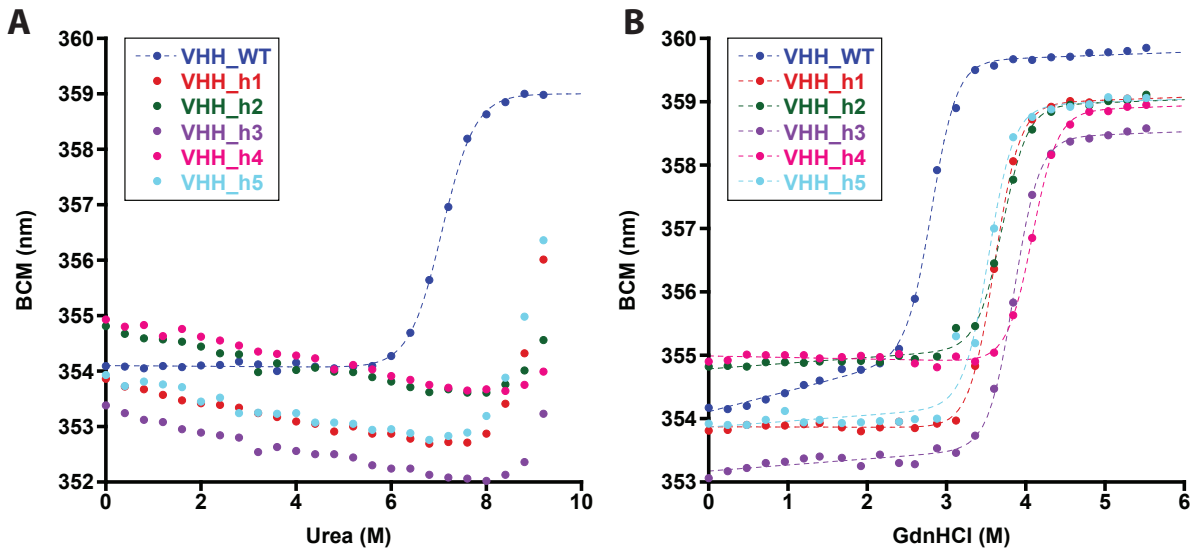

Fig. S10. Representative chemical denaturation curves of VHH_WT, VHH_h1-h5. (A) Urea denaturation. **(B)** GndHCl denaturation. Fits were done using Kaleidagraph. Average ΔG is listed in table S6.

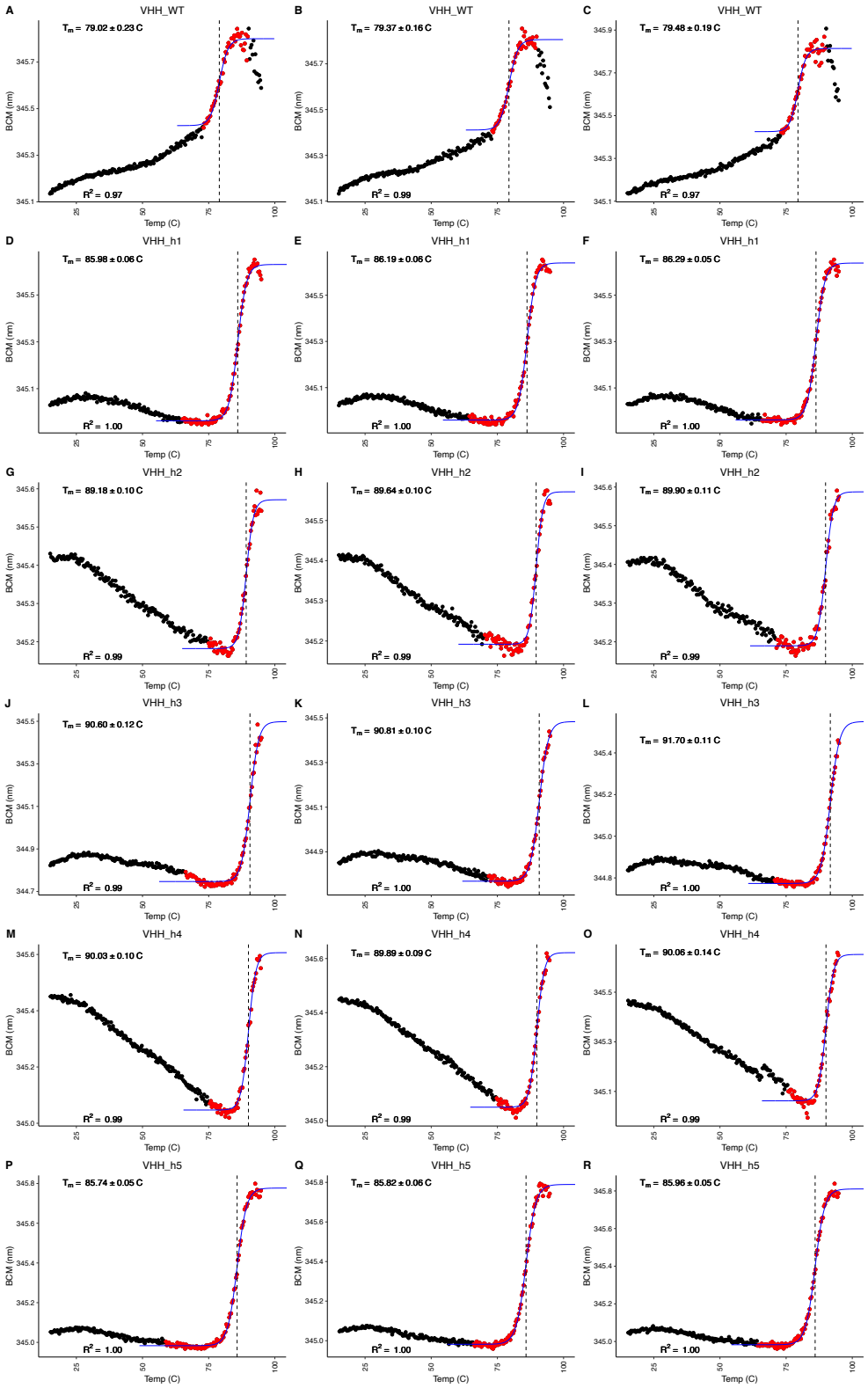

Fig. S11. T_m determination based on Barycentric Mean calculation from Intrinsic Tryptophan Fluorescence (ITF) during a temperature ramp for VHH_WT, VHH_h1-VHH_h5.

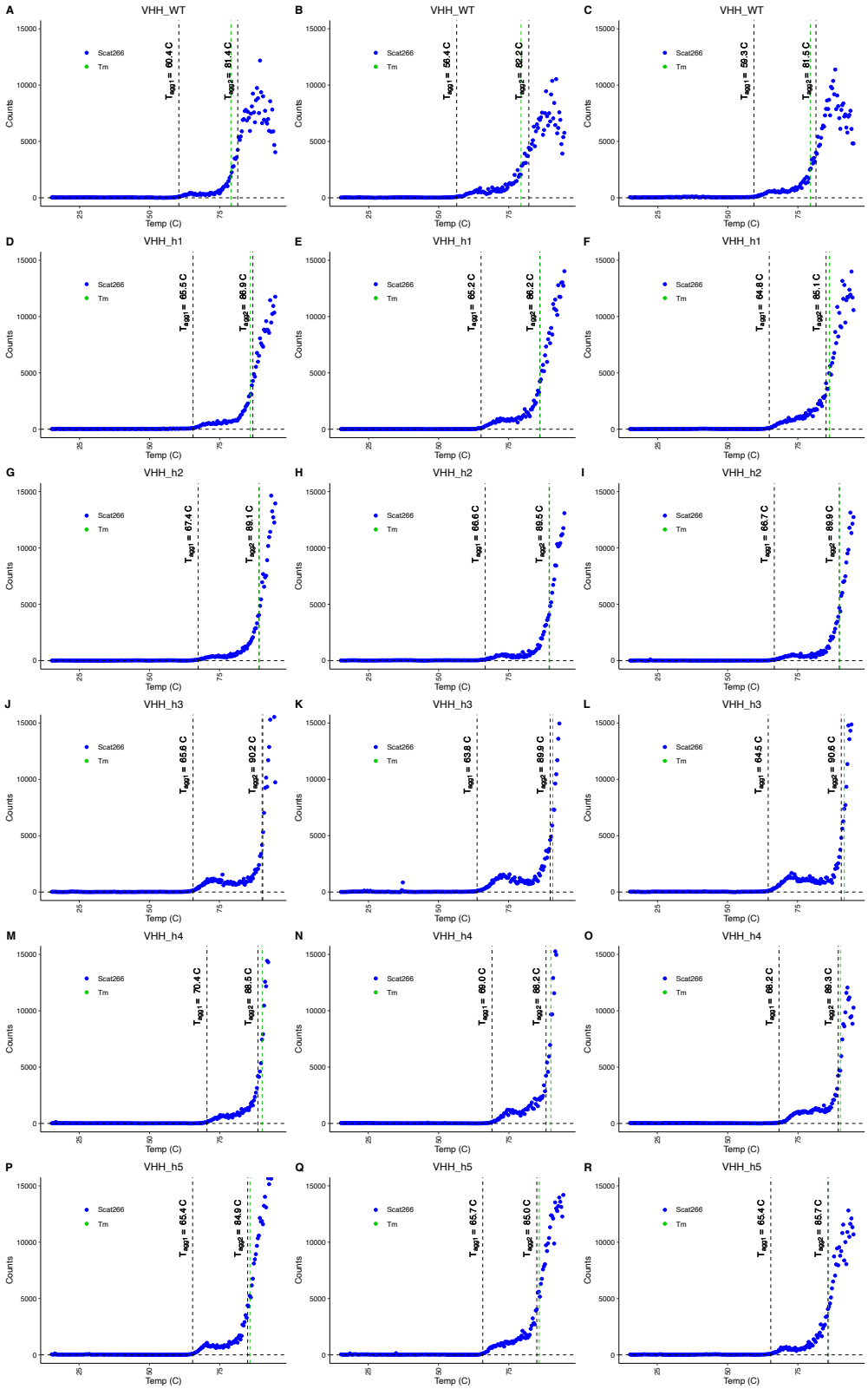

Fig. S12. T_{agg} determination based on Scatting at 266 nm from Right Angle Light Scattering (RALS) during a temperature ramp for VHH_WT, VHH_h1-VHH_h5.

a)

Protein	MW_{calc} (kDa) Protein
hVsig4 (20-137)	14.46
VHHh1	14.85
VHHh2	14.76
VHHh3	14.77
VHHh4	14.80
VHHh5	14.70

b)

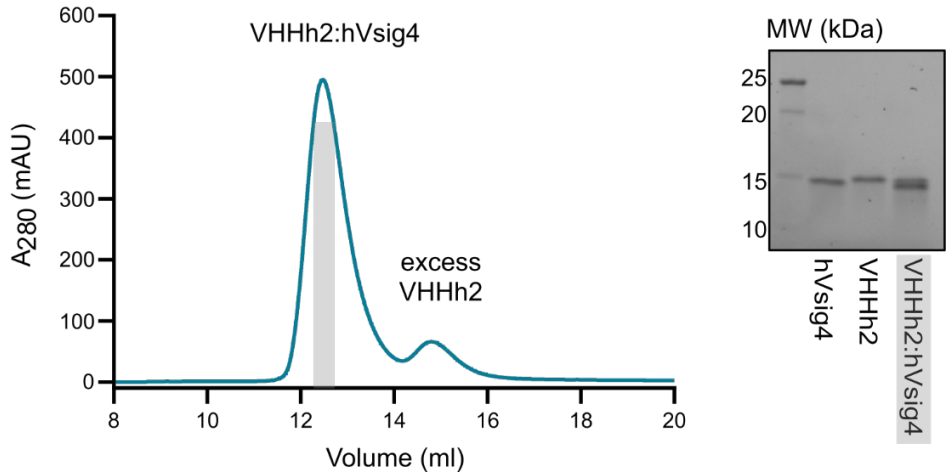

Fig. S13. Representative SEC elution profiles for VHH_h2:hVsig4 complex reconstitution. (A) Overview of molecular masses of all the VHHs and hVsig4. **(B)** Representative SEC elution profile for the purification of the VHH_h2:hVsig complex using excess of VHH_h2 on a Superdex 75 Increase 10/300 GL column and representative SDS-PAGE.

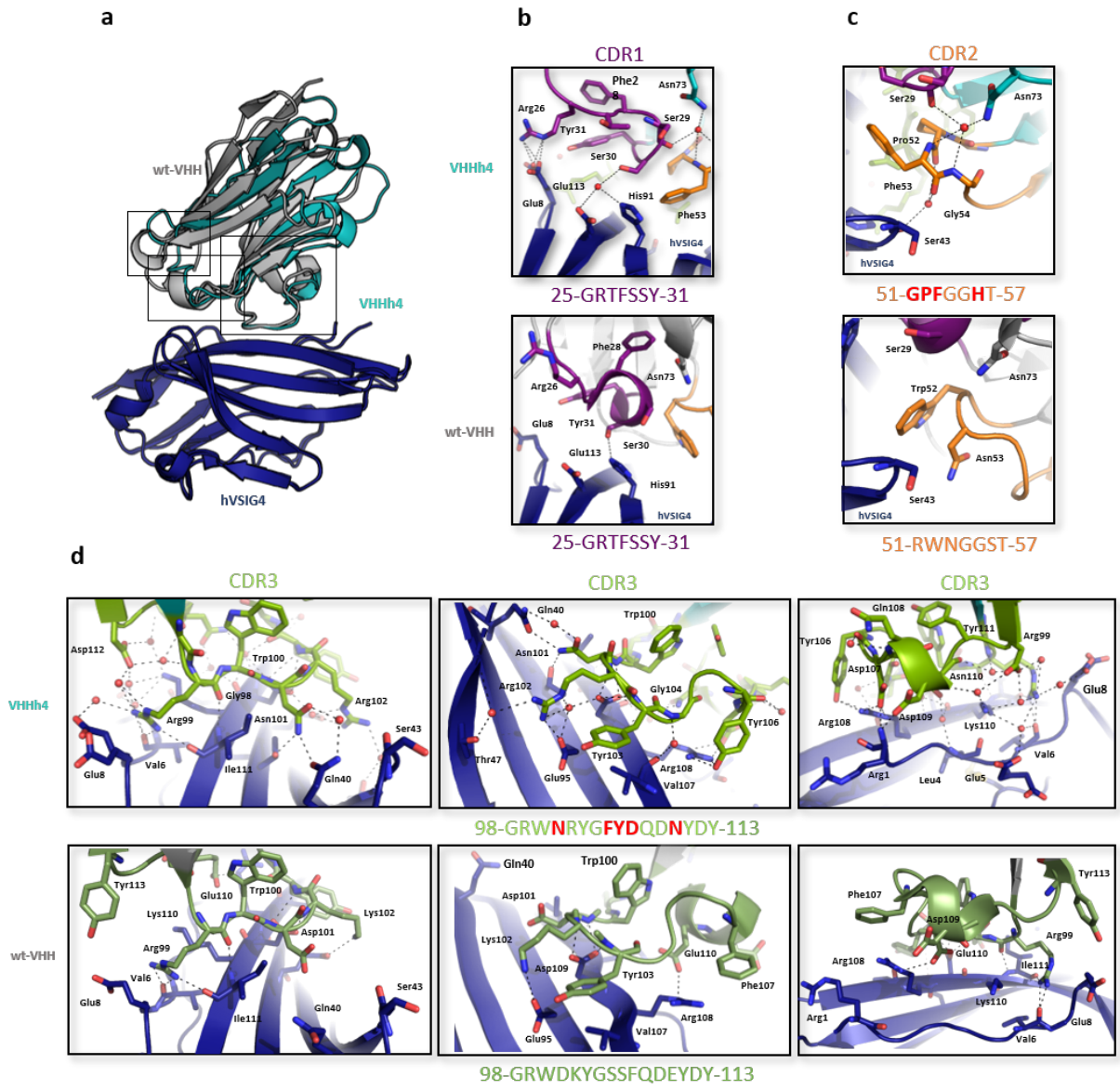

Fig. S14. Structure of the hVsig4:VHH_h4 complex compared to the hVsig4:VHH_WT complex. **(A)** Cartoon representation of the determined X-ray structure for VHH_h4 fragment in complex with hVsig4 superimposed to hVsig4:VHH_WT complex (PDB 5IML) based on the structural alignment of the two hVsig4 structures. VHH_h4 is colored in teal, VHH_WT in grey and hVsig4 in dark blue. **(B)** Details of the hVsig4:VHH_h4 (up) and hVsig:VHH_WT (down) interface focusing on CDR1 loop. CDR1 loops of VHHh4 and VHH_WT are coloured in deep purple. **(C)** Details of the hVsig4:VHH_h4 (up) and hVsig:VHH_WT (down) interface focusing on CDR2 loop. CDR2 loops of VHH_h4 and VHH_WT are coloured in orange. **(D)** Details of the hVsig4:VHH_h4 (up) and hVsig:VHH_WT (down) interface focusing on CDR3 loop with 3 different perspectives. Selected interface residues are labelled and shown as sticks. CDR3 loops of VHH_h4 and VHH_WT are coloured in green (split pea). Dashed lines represent salt bridges and hydrogen bonds. Red spheres represent water molecules which are part of the interface.

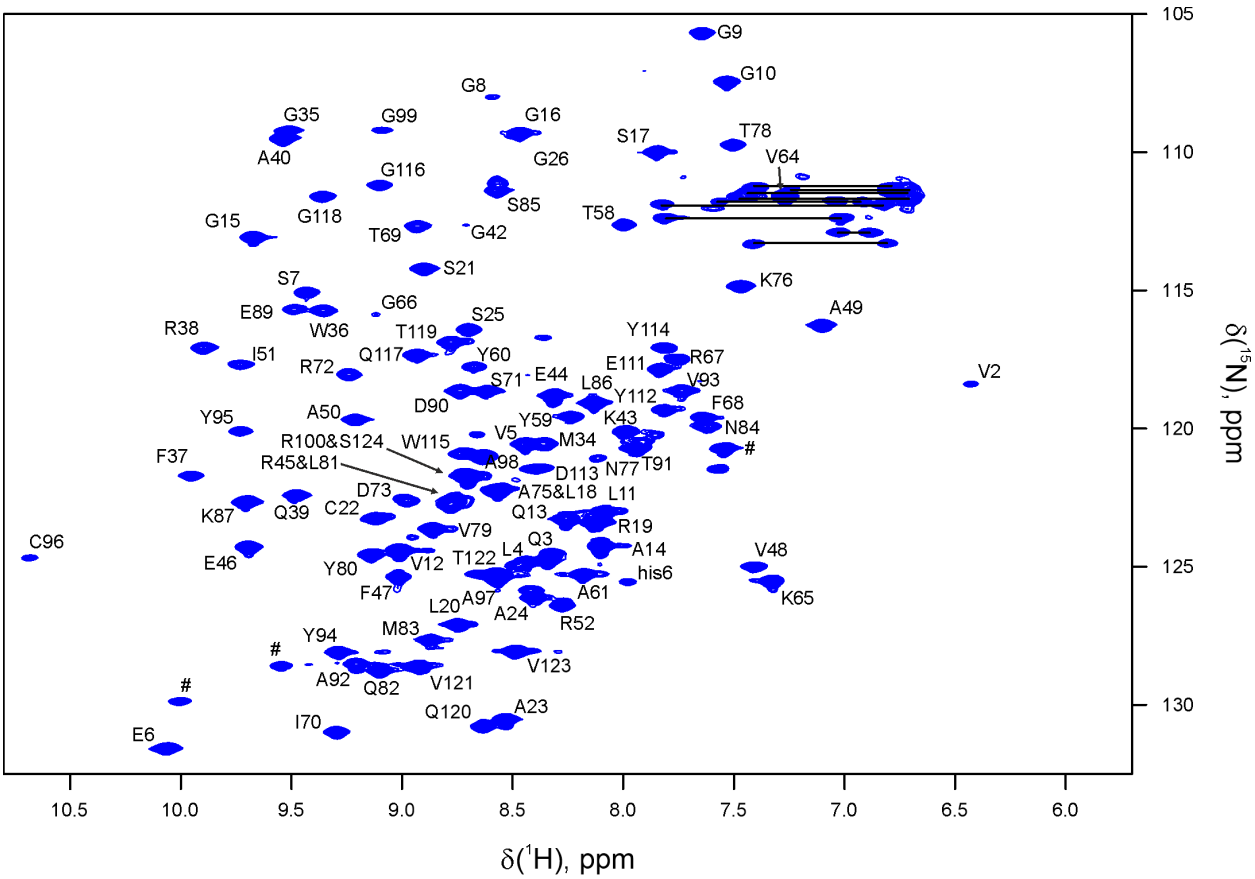

Fig. S15. [^{1}H,^{15}N] HSQC spectrum of VHH_WT. The labels show assigned backbone amide resonances, tryptophan $N_{\varepsilon1}H_{\varepsilon1}$ indoles (#), a His-tag peak (his6), and sidechain NH_2 resonances of Asn and Gln residues (horizontal lines). The experiments were performed in 20 mM sodium phosphate 50 mM NaCl pH 6.5 at 313 K.

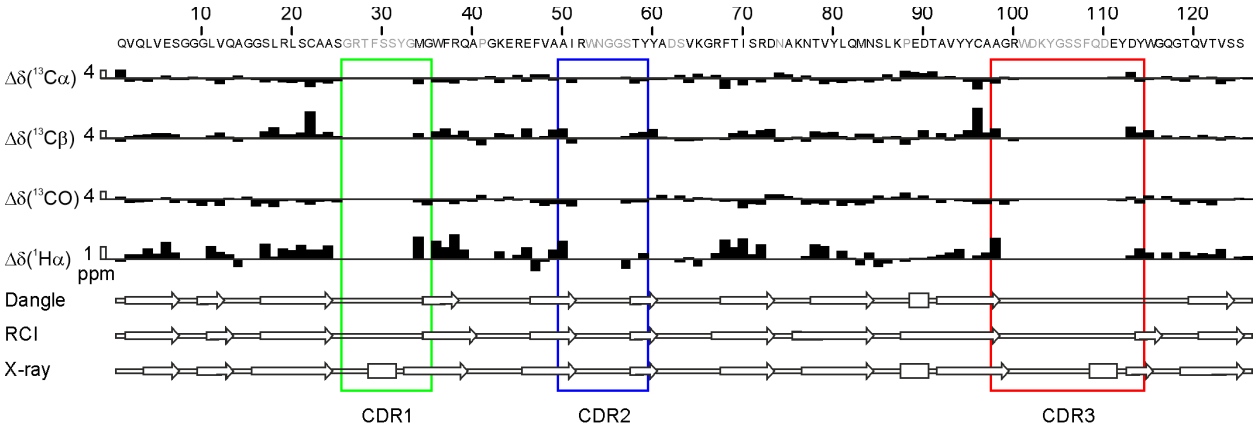

Fig. S16. Extent of the NMR backbone assignment and secondary structure prediction of VHH_WT. Threshold deviations from random-coil ^{13}Cα, ^{13}Cβ, ^{13}CO, and ^{1}Hα chemical shifts (filled bars), with the leading open bars for scale (values in ppm). The secondary structure (rectangles – α helices, arrows – β strands) predicted by DANGLE, RCI, or seen in the X-ray structure of the VHH_WT bound to mouse Vsgi4 (5immBA). The residues that exhibited no backbone amide resonances in the HSQC spectrum are in grey.

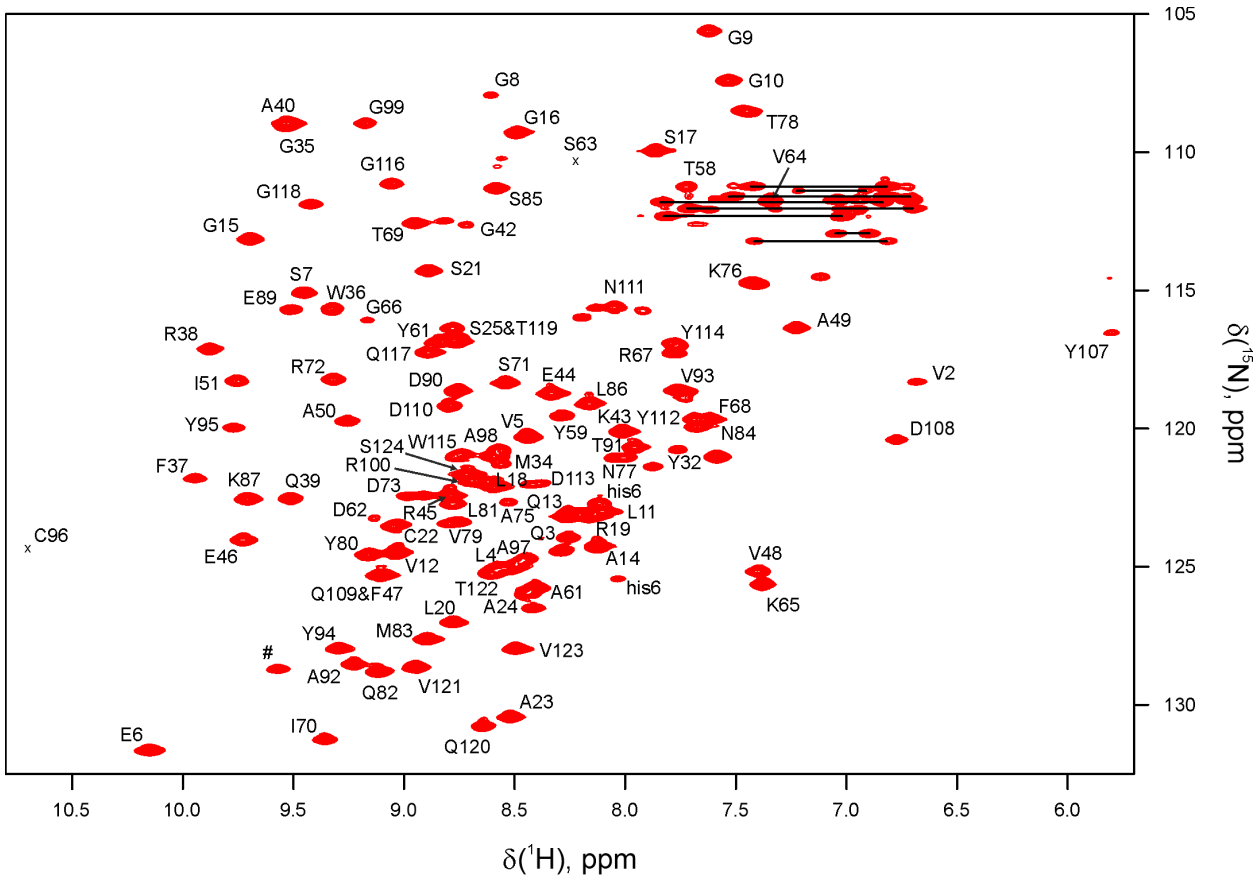

Fig. S17. [^{1}H,^{15}N] HSQC spectrum of VHH_h4. The labels show assigned backbone amide resonances, tryptophan $N_{\varepsilon1}H_{\varepsilon1}$ indole (#), His-tag peaks (his6), and sidechain NH_2 resonances of Asn and Gln residues (horizontal lines). Positions of S63 and C96 backbone amide signals (not seen at this contour level) are indicated by crosses. The experiments were performed in 20 mM sodium phosphate 50 mM NaCl pH 6.5 at 313 K.

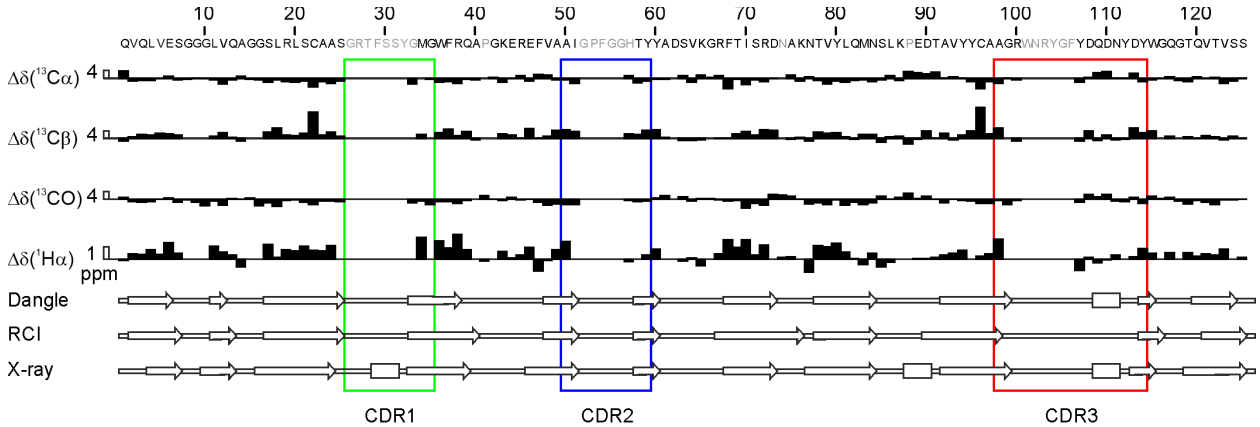

Fig. S18. Extent of the NMR backbone assignment and secondary structure prediction of VHH_h4. Threshold deviations from random-coil ^{13}Cα, ^{13}Cβ, ^{13}CO, and ^{1}Hα chemical shifts (filled bars), with the leading open bars for scale (values in ppm). The secondary structure (rectangles – α helices, arrows – β strands) predicted by DANGLE, RCI, or seen in the X-ray structure of the VHH_WT bound to mouse Vsgi4 (5immBA). The residues that exhibited no backbone amide resonances in the HSQC spectrum are in grey.

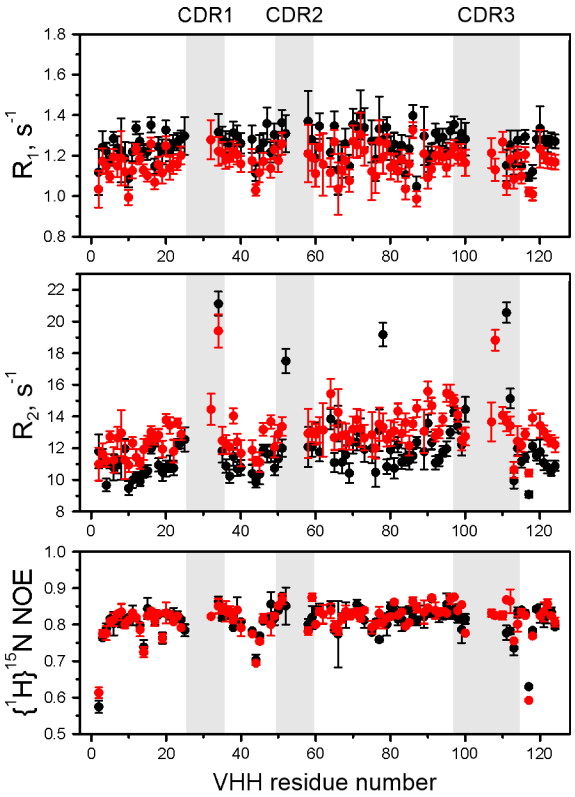

Fig. S19. ^{15}N NMR relaxation parameters of VHHs. Spin-lattice (R_1) and spin-spin (R_2) relaxation rates, and heteronuclear steady-state nuclear Overhauser effect ({^{1}H}-^{15}N NOE) of the backbone amide atoms of VHH_WT (black) and VHH_h4 (red). The grey areas indicate CDR regions. Experiments were performed in 20 mM NaPi 50 mM NaCl pH 6.5 at 313 K.

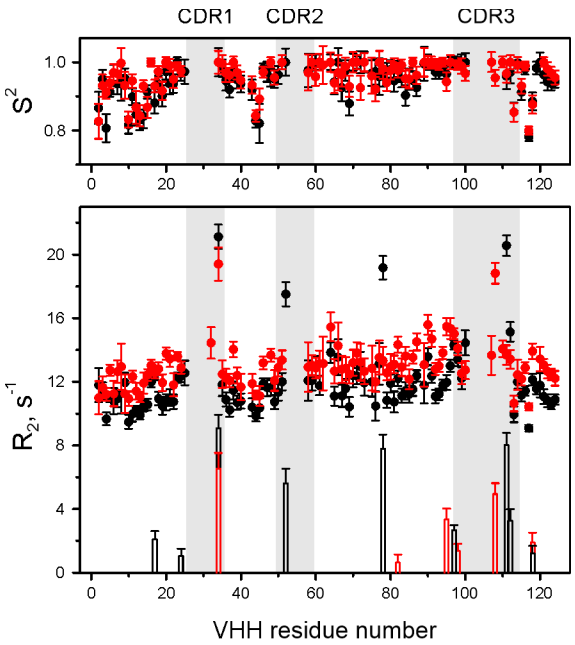

Fig. S20. Backbone dynamics of VHHs. (top) S^2 order parameters for the N-H vectors obtained from the model-free analysis of the NMR relaxation data in fig S19. (bottom) Measured R_2 relaxation rates (circles) and $R_{2,ex}$ exchange contributions obtained from the model-free analysis (bars). The data for the VHH_WT and VHH_h4 are in black and red, respectively. The grey areas indicate CDR regions. S2 metric indicates very limited ps-ns dynamics, with the smallest values for the N-terminus and loops centered on residues 10, 44, and 117 (top). Interestingly, the few VHH_WT CDR residues that do exhibit HSQC peaks show considerable exchange contributions to transverse relaxation rates (R2,ex), suggesting that they undergo a conformational exchange on the µs-ms timescale (bottom). The R2,ex contributions are reduced in the VHH_h4 (bottom), suggesting a much less extensive conformational exchange of the mutant CDRs, which explains its more favorable spectral properties.

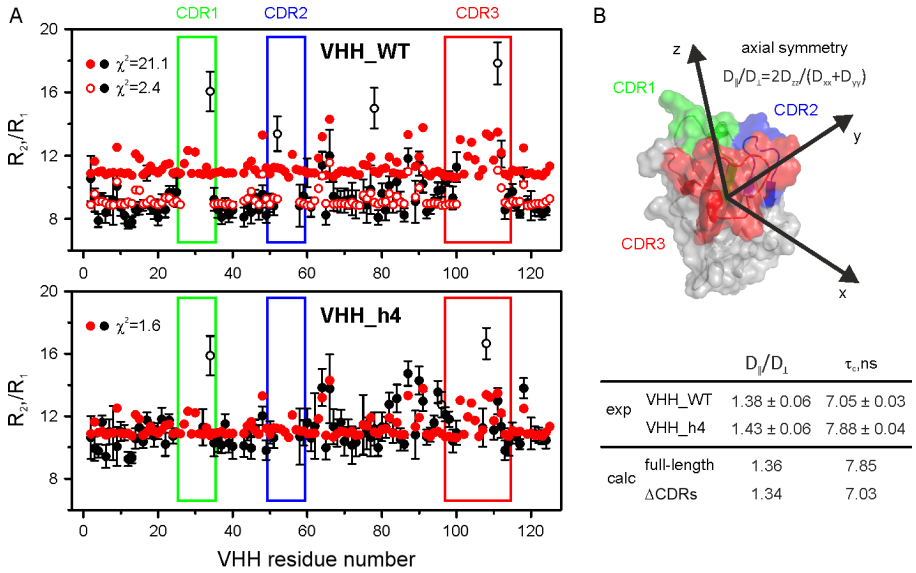

		$D_{\parallel}/D_{\perp}$	τ_c,ns
exp	VHH_WT	1.38 ± 0.06	7.05 ± 0.03
	VHH_h4	1.43 ± 0.06	7.88 ± 0.04
calc	full-length	1.36	7.85
	ΔCDRs	1.34	7.03

Fig. S21. Hydrodynamic properties of VHHs. (**A**) Measured (black) and predicted (red) ratios of ^{15}N R_1 and R_2 NMR relaxation rates for the VHH_WT (top) and VHH_h4 (bottom). R_2/R_1 values were calculated from the X-ray structure of the full-length VHH_WT or with the CDRs removed (filled and open red circles, respectively). VHH residues with R_2 exchange contributions (black open circles) were excluded from the χ^2 calculations. (**B**) Orientation of the diffusion tensor (coordinate system) in the VHH molecular frame. The structure of the VHH_WT is taken from the X-ray structure of its complex with the mouse Vsgi4 (5immBA), with CDRs indicated. The relaxation properties of both VHHs are well accounted for by an axially symmetric diffusion model, with the diffusion tensor parameters given in (B). Calculated from the X-ray structure of VHH bound to mouse Vsgi4, the hydrodynamic parameters of VHH_h4 are in excellent agreement with those derived from experiment: closely matching values of rotational correlation time (τc) and high similarity of experimental and calculated R2/R1 profiles (χ2 = 1.6) are particularly noteworthy (A, bottom). At the same time, the measured R2/R1 and experimentally derived τc values for the VHH_WT are considerably lower than expected (A, top), indicating a faster molecular tumbling compared to VHH_h4. To simulate a molecular system where conformationally exchanging CDR loops do not contribute to the overall protein tumbling, we removed the VHH_WT CDR residues that show no HSQC peaks from the X-ray structure and re-calculated the hydrodynamic properties. Both R2/R¬ and τc parameters of this reduced set (ΔCDRs) are in excellent agreement with the experimental VHH_WT values (A, top). Overall, it appears that free VHH_h4 in solution maintains the bound-like protein conformation, with closely packed CDR loops undergoing limited motion, while the CDRs of VHH_WT are largely disordered and involved in extensive conformational exchange.

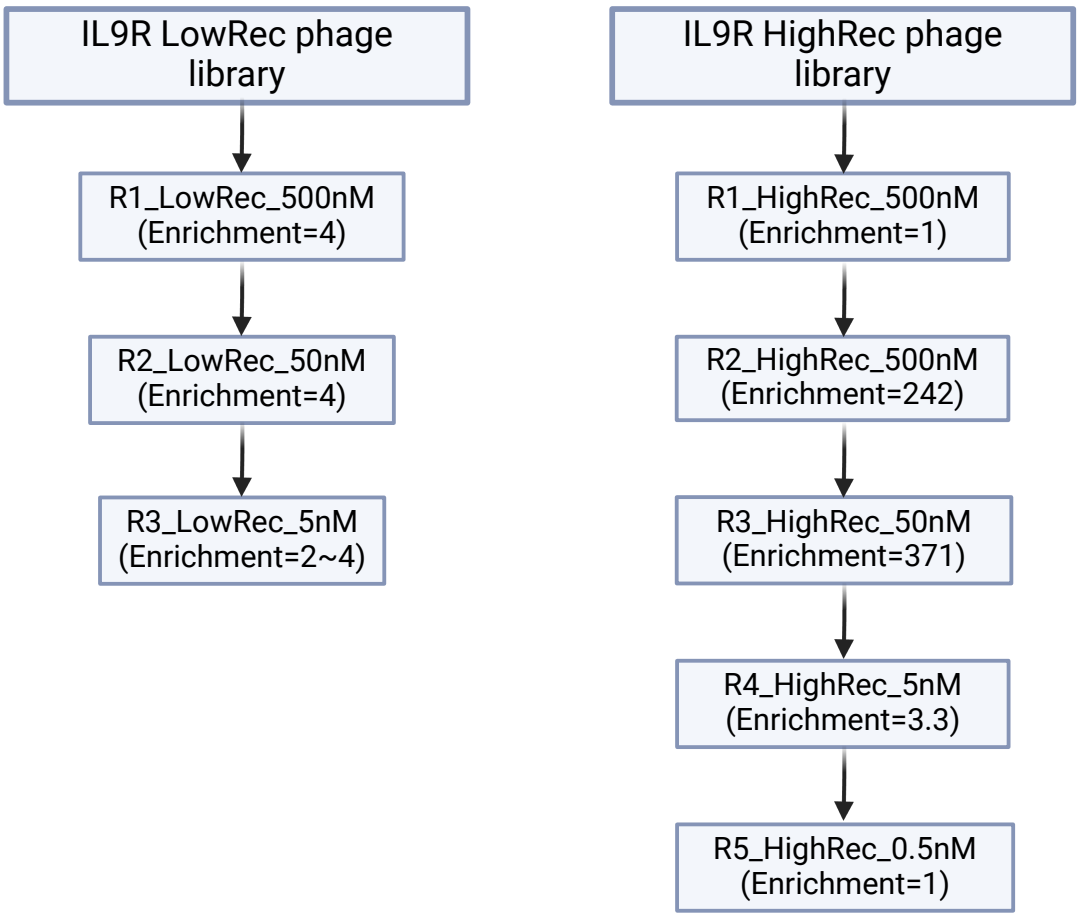

Fig. S22. Phage display selection rounds hIL-9Rα library. Identical library with high and low recombination rate during cloning. Graphical designs were created with BioRender.com.

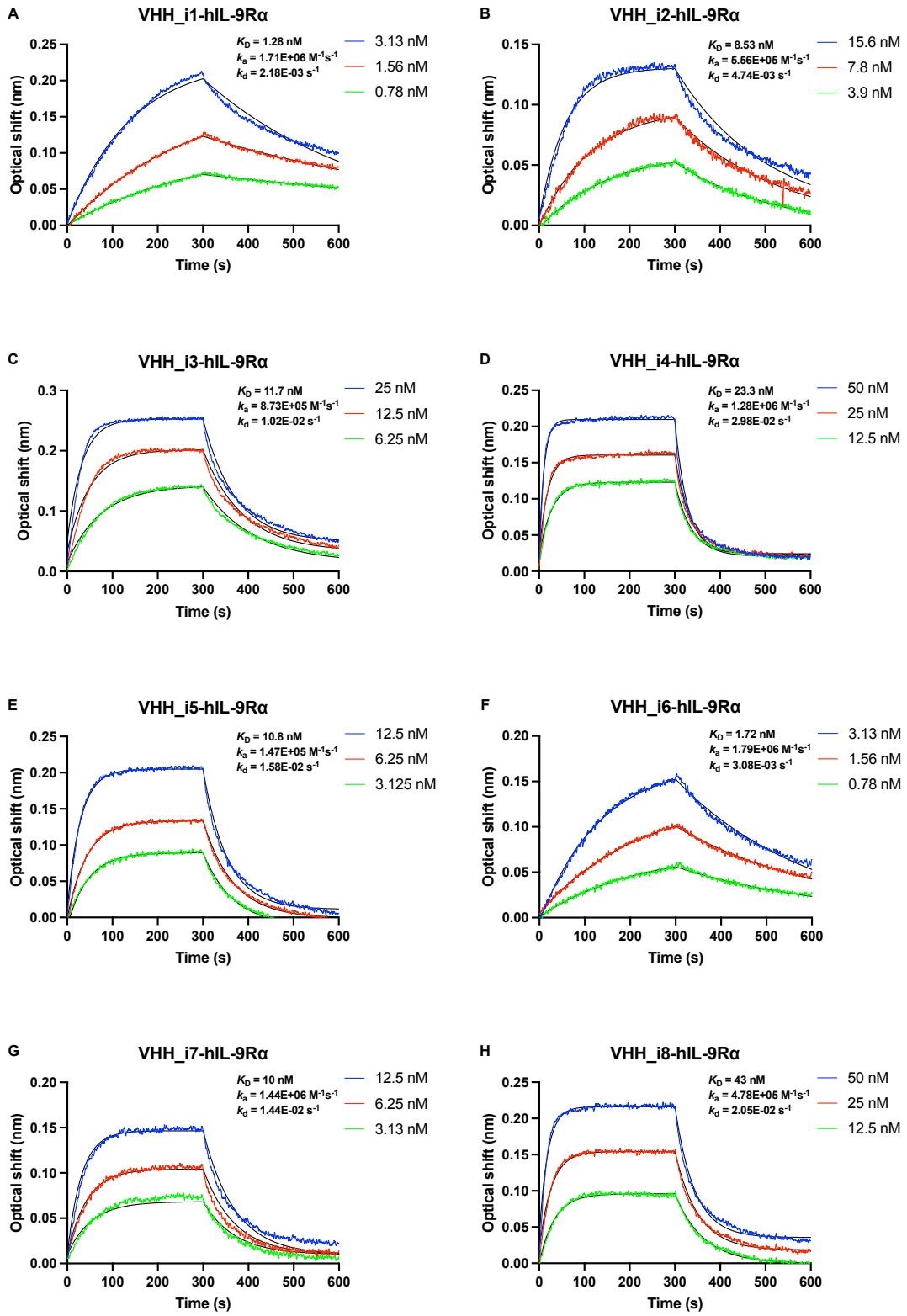

Fig. S23. The binding curves of VHH_i1-VHH_ i8 against hIL-9Rα (BLI).

Supplementary Tables

Table S1: 36 unique sequences of mVsig4 hits with average of AlphaScreen signal/noise (S/N) ratio

Sequence alignment	Average of AS S/N
QVQLVESGGGLVQAGGSLRLSCAASGRTFSSYGMGWFRQAPGKEREFVAAIRWNGGSTYYADSVKGRFTISRDNAKNTVYLQMNSLKPEDTAVYYCAAGRWDKYGSSFQDEYDYWGQGTQVTVSS	21.57
.....S.....RH.AYD.Y.....	46.17
.....NY.....RH.AYD.Y.....	22.33
.....VE.....RH.AYD.Y.....	18.59
.....VE.....LF..FD..N.....	16.27
.....VE.....LF.KYD..N.....	16.21
.....VE.....I.....LF..YD..N.E.....	13.93
.....VE.....LF..YD..N.....	12.06
.....VE.....LF..YD..N.E.....	12.02
.....VE.....LF..FD..N.E.....	11.35
.....RY.....LF..FD..N.E.....	11.01
.....R.....VE.....LF..FD..N.E.....	10.70
.....V.....LF.KYD..N.E.....	10.39
.....VE.....LF.KFD..N.E.....	8.78
.....L.....VE.....LF..FD..N.E.....	8.49
.....VE.....T.....LF..YD..N.E.....	8.41
.....VE.....LF.KYD..N.E.....	7.27
.....T.....	5.78
.....DY.....LF..YD..N.E.....	2.13
.....DE.....LF..YD..N.E.....	1.94
.....L...VE.....LF..FD..NFE.....	1.42
.....DE.....LF..FD..N.E.....	1.37
.....SEY.YA.....VWN..FGE.W..S.....	1.34
.....K...YY.....F..AFE.ES.....	1.31
.....SA.....LF..FD..N.E.....	1.30
.....G.D.EY.....RH.AYD.Y.....	0.90
.....G.D.EY.....L.....RH.AYD.Y.....	0.72
.....SPD.NL.....SLRF.AAL.E.LE.....	0.65
.....SEY.YG.....VWN..FGE.W..S.....	0.59
.....SEY.YG.....RYF.NFD.N..E.....	0.54
.....SEY.YA.....PVNF..YYE.YD.N.....	0.52
.....SPY.Y.....AEY..YA..YDFE.....	0.49
.....DPY.DV.....NI..NYD.IL.E.....	0.41
.....A.DY.....FF.YDE.ND.K.....	0.40
.....SPS.SR.....F..AFE.ES.....	0.35
.....SPY.DY.....YR..WE.I.E.....	0.35
.....HPY.SL.....VWE..Y.S.E.FE.....	0.35

Table S2: 12 sequences of mVsig4 hits selected for the BLI off-rate test

Sequence alignment	k_d (s^{-1})
QVQLVESGGGLVQAGGSLRLSCAASGRTFSSYGMGWFRQAPGKEREFVAAIRWNGGSTYYADSVKGRFTISRDNAKNTVYLQMNSLKPEDTAVYYCAAGRWDKYGSSFQDEYDYWGQGTQVTVSS	6.38E-03
.....VE.....LF..YD..N.....	4.22E-03
.....VE.....LF..YD..N.E.....	4.77E-03
.....VE.....LF..FD..N.....	4.80E-03
.....VE.....LF..FD..N.E.....	5.13E-03
.....VE.....LF.KYD..N.....	6.13E-03
.....VE.....LF.KYD..N.E.....	6.70E-03
.....V.....LF.KYD..N.E.....	6.75E-03
.....RY.....LF..FD..N.E.....	7.32E-03
.....VE.....LF.KFD..N.E.....	7.89E-03
.....NY.....RH.AYD.Y.....	8.01E-03
.....S.....RH.AYD.Y.....	8.26E-03
.....VE.....RH.AYD.Y.....	8.77E-03

Table S3. Biophysical characterization data of VHH_m1-VHH_m4.

Name	CDR2	CDR3	K_D BLI (nM) (mVsig4)	K_D SPR (nM) (mVsig4)	T_m (°C)	T_{agg} (°C)	ΔG_{Urea} (kcal/mol)	ΔG_{GdnHCl} (kcal/mol)
VHH_WT	AI**RWN**G**GS**TY	GR**WDKY**G**SSFQDE**Y**D**Y	0.9	0.2	80.0	80.7	-10.2	-10.7
VHH_m1	.....VE..	....LF..YD..N.D.	1.0	1.2	84.6	86.2	☆	-12.3
VHH_m2	.....VE..	....LF..YD..N.E.	2.7	0.5	85.9	86.5	☆	-12.5
VHH_m3	.....VE..	....LF..FD..N.D.	2.4	2.0	84.0	86.0	☆	-12.3
VHH_m4	.....VE..	....LF..FD..N.E.	2.5	0.7	86.6	89.5	☆	-12.4

(Note: CDR definition: AbM, ☆ means it was not fully denatured under the most extreme conditions)

Table S4: 112 unique sequences of hVsig4 hits with average of ELISA signal/noise (S/N) ratio

Sequence alignment	Average of ELISA S/N
QVQLVESGGGLVQAGGSLRLSCAASGRTFSSYGMGWFRQAPGKEREFVAAIRWNGGSTYYADSVKGRFTISRDNAKNTVYLQMNSLKPEDTAVYYCAAGRWDKYGSSFQDEYDYWGQGTQVTVSS	4.33
.....GPF..H.....NR..FYD..N.....	37.30
.....GPF.....NR..FED..NF.....	35.92
.....GPF..I.....NR..FED..NF.....	35.66
.....PF..D.....NR..FED..NF.....	34.98
.....PF.NY.....NR..FED..NF.....	34.87
.....GPF.SL.....NR..FED..NF.....	34.18
.....SPF..T.....NR..FED..NF.....	33.44
.....PF.AN.....NR..FYD..N.....	32.50
.....GPF.NG.....A.....NR..FED..NF.....	32.00
.....GPF.DK.....NR..FED..NF.....	31.56
.....SPF..N...S.....NR..FED..NF.....	31.22
.....PF..D.....NR..FYD..N.....	31.22
.....GPF.....NR..FEDR.NF.....	31.00
.....APF.YT.....NR..FED..NF.....	29.28
.....SPF..N.....NR..FED..NF.....	29.06
.....GPF..T.....T....NR..FYE..N.....	28.69
.....GPF.SR.....NR..FED..NF.....	27.89
.....GPF..Y.....NR..FYD..N.....	27.56
.....GPF.R.....I.....NR..FED..NF.....	27.41
.....R..G.....NR..FED..NF.....	27.06
.....GPF..T.....NR..EQD.YN.E.....	26.50
.....SPF..A.....NR..FED..NF.....	26.34
.....GPF.DR.....NY..QYE.TS.....	25.48
.....NPF..H.....NR..FED..NF.....	25.41
.....GPF.RG.....NR..FED..NF.....	25.19
.....NPF..Y.....NR..FYD..N.....	24.24
.....SPF..Q.....NR..FED..NF.....	23.75
.....SPF.EN.....NR..FYD..N.....	23.33
.....APF.LT.....NR..FED..NF.....	22.22
.....GPF.DR.....NY..QFD.YS.E.....	21.97
.....VPF..D.....NR..FYD..N.....	21.70
.....PF.WD.....NR..FED..NF.....	21.37
.....FS.AY.....NR..FED..NF.....	21.03
.....GPF.YE.....NR..FED..NF.....	20.70
.....APF.DR.....RY..EDD.EN.E.....	20.52
.....TPF.EW.....NR..FED..NF.....	20.15
.....TPF.SL.....NR..FED..NF.....	19.19
.....GPY.SY.....NR..FED..NF.....	19.07
.....SPF..R.....NR..FED..NF.....	18.94
.....SPY..T.....NR..FED..NF.....	18.51
.....APF.YD.....NR..FED..NF.....	18.41
.....APF.HK.....NR..EQD.YN.E.....	18.13
.....TPF.D.....NR..FED..NF.....	17.63
.....SPF.RY.....NR..FED..NF.....	17.38
.....VE.....NY..FTD..NFE.....	16.93
.....APY.SY.....NR..FED..NF.....	16.91
.....VE.....LF..YD..N.E.....	16.51
.....S.R.AR.....NR..FED..NF.....	15.82
.....SPF..W.....NR..FED..NF.....	15.63
.....GPF.SY.....NF..FED..NF.....	15.15
.....SPF.SH.....NR..FED..NF.....	14.84
.....SPF.SH.....NR..FYD..N.....	14.81
.....APF.L.....NR..FED..NF.....	14.74
.....SPF..R.....NR..FYD..N.....	14.66
.....SPY.SW.....NR..FED..NF.....	13.78
.....VPY.RY.....NR..FED..NF.....	13.74
.....SPF.SL.....NR..FED..NF.....	13.70
.....SPF.YK.....NR..FED..NF.....	13.63
.....SSF.RR.....NR..FED..NF.....	12.56
.....TPY..Y.....NR..FED..NF.....	12.52
.....GGY.KY.....M.....NR..FYD..N.....	12.48
.....SPF.SY.....LRF.YYD.EN.E.....	12.30
.....APY.DY.....NR..FED..NF.....	12.30
.....N...K.....NR..FYD..N.....	12.28
.....APF.R.....LRF.YYD.EN.E.....	11.96
.....SPF..R.....NY..FTD..NFE.....	11.93
.....VE.....LF..FD..N.E.....	11.92
.....SPF..L.....NR..FYD..N.....	11.88
.....TPF.VE.....YR..FED..NF.....	11.82
.....SPY.YY.....L.....NR..FED..NF.....	11.67
.....NPY.RI.....NR..FYD..N.....	11.65
.....SPF.H.....NR..FED..NF.....	11.38
.....PF.WD.....NR..FYE..N.....	11.33
.....GPY..T.....NR..PTD.EN.....	11.30
.....TPF.IG.....NR..FED..NF.....	11.22
.....SYD.SY.....RY..EDD.RN.E.....	10.44
.....VPY.RR.....NR..FED..NF.....	10.29
.....VPY.TR.....NR..FED..NFG.....	10.26
.....GPF..R.....NY..FTD..NFE.....	10.03
.....VE.....NL..KYE..S.....	9.96
.....APF.RH.....NR..FYD..N.....	9.93
.....S.NQ.....NR..FED..NFG.....	9.85

.....	NPY.RR	NR..FED..NF.....	9.63
.....	SPF.YT	NR..FED..NF.....	9.59
.....	NPY.RR	NR..FED..NF....R..R.....	9.44
.....	SPF.VT	NR..FED..NFG.....	9.30
.....	GPF.RQ	NR..FED..NFG.....	9.28
.....	PF	NY..FTD..NFE.....	9.11
.....	APY.SF	NR..FED..NF.....	8.52
.....	W.....	SPF..N	NR..FED..NF.....	8.48
.....	SPF..Y	LRF.YYD.EN.E.....	8.37
.....	APF.YE	RY..EDD.EN.E.....	7.97
.....	YPY.NR	NR..FED..NF.....	7.44
.....	SPF.YQ	LRF.YYD.EN.E.....	7.15
.....	NPF.QN	NF..YYE.KNH.....	6.52
.....	SPW.YA	NR..FED..NFG.....	6.38
.....	TPF.YQ	NR..FYD..N.....	6.26
.....	SPF.RQ	NR..AND....S.....	6.22
.....	PF.SE	NYF.PYD..N.E.....	5.91
.....	GPF.SF	RY..EDD.RN.E.....	5.19
.....	SPF.EN	NY..FTD..NFE.....	4.11
.....	GPF.S	NF..YYE.KNH.....	4.04
.....	NPF..Y	RY..AND....E.....	3.67
.....	SPF..V	NNR..FYS....E.....	3.30
.....	SPF.EL	HYF.E.D.EN.E.....	2.96
.....	QPF.H	LN..R-E..Q.E.....	2.94
.....	DY	LF..YD..N.E.....	2.69
.....	SPF.LE	LF.KYD..N.E.....	2.22
.....	SPW.YK	NR..PTD.EN.E.....	1.82
.....	SPF.LT	NY..FTD..NFE.....	1.81
.....	SPF..R	LF..YD..N.E.....	1.00
.....	YPY.NY	NF..YED.NL.E.....	0.81

Table S5: 56 sequences of hVsig4 hits selected for the BLI off-rate test

Sequence alignment	k_d (s^{-1})
QVQLVESGGGLVQAGGSLRLSCAASGRTFSSYGMGWFRQAPGKEREFVAAIRWNGGSTYYADSVKGRFTISRDNAKNTVYLQMNSLKPEDTAVYYCAAGRWDKYGSSFQDEYDYWGQGTQVTVSS	4.14E-02
.....SPF..N.....NR..FED..NF.....	7.48E-03
.....GPF..T.....NR..EQD.YN.E.....	8.59E-03
.....GPF.YE.....NR..FED..NF.....	1.03E-02
.....GPF.R.....I.....NR..FED..NF.....	1.19E-02
.....SPF..W.....NR..FED..NF.....	1.24E-02
.....GPF.RG.....NR..FED..NF.....	1.26E-02
.....GPF..T.....T....NR..FYE..N.....	1.30E-02
.....SPF..Q.....NR..FED..NF.....	1.30E-02
.....TPF.SL.....NR..FED..NF.....	1.31E-02
.....SPF.RY.....NR..FED..NF.....	1.36E-02
.....PF.NY.....NR..FED..NF.....	1.38E-02
.....NPF..H.....NR..FED..NF.....	1.38E-02
.....PF.WD.....NR..FED..NF.....	1.40E-02
.....SPF..N...S.....NR..FED..NF.....	1.43E-02
.....GPF..H.....NR..FYD..N.....	1.45E-02
.....APF.YE.....RY..EDD.EN.E.....	1.45E-02
.....APF.YD.....NR..FED..NF.....	1.46E-02
.....APF.LT.....NR..FED..NF.....	1.48E-02
.....APF.YT.....NR..FED..NF.....	1.49E-02
.....GPF.NG.....A.....NR..FED..NF.....	1.51E-02
.....PF..D.....NR..FYD..N.....	1.51E-02
.....GPF.....NR..FEDR.NF.....	1.51E-02
.....SPF..A.....NR..FED..NF.....	1.51E-02
.....GPF.SY.....NF..FED..NF.....	1.51E-02
.....SPF..T.....NR..FED..NF.....	1.53E-02
.....GPF.....NR..FED..NF.....	1.55E-02
.....R..G.....NR..FED..NF.....	1.56E-02
.....GPF.SR.....NR..FED..NF.....	1.59E-02
.....FS.AY.....NR..FED..NF.....	1.59E-02
.....SPF..R.....NR..FED..NF.....	1.63E-02
.....APF.HK.....NR..EQD.YN.E.....	1.74E-02
.....GPF.DK.....NR..FED..NF.....	1.75E-02
.....GPF..I.....NR..FED..NF.....	1.76E-02
.....GPF.SL.....NR..FED..NF.....	1.81E-02
.....PF..D.....NR..FED..NF.....	1.84E-02
.....VPF..D.....NR..FYD..N.....	1.85E-02
.....S.R.AR.....NR..FED..NF.....	1.85E-02
.....SPF.EN.....NR..FYD..N.....	1.91E-02
.....PF.AN.....NR..FYD..N.....	1.93E-02
.....GPF..Y.....NR..FYD..N.....	1.96E-02
.....VE.....NY..FTD..NFE.....	2.43E-02
.....SPY..T.....NR..FED..NF.....	2.51E-02
.....GPY.SY.....NR..FED..NF.....	2.53E-02
.....NPY.RR.....NR..FED..NF.....	3.30E-02
.....VPY.RR.....NR..FED..NF.....	3.41E-02
.....NPY.RI.....NR..FYD..N.....	3.69E-02
.....TPF.D.....NR..FED..NF.....	4.09E-02
.....APY.SY.....NR..FED..NF.....	4.41E-02
.....GPF.DR.....NY..QYE.TS.....	4.81E-02
.....TPF.EW.....NR..FED..NF.....	5.29E-02
.....DY.....LF..YD..N.E.....	5.35E-02
.....VE.....LF..YD..N.E.....	6.01E-02
.....APF.DR.....RY..EDD.EN.E.....	6.35E-02
.....NPF..Y.....NR..FYD..N.....	6.98E-02
.....GPF.DR.....NY..QFD.YS.E.....	8.23E-02
.....VPY.TR.....NR..FED..NFG.....	1.15E-01

Table S6. Biophysical characterization data of VHH_h1-VHH_h5.

Name	CDR2	CDR3	K_D BLI (nM) (hVsig4)	K_D SPR (nM) (hVsig4)	T_m (°C)	T_{agg} (°C)	ΔG_{Urea} (kcal/mol)	ΔG_{GdnHCl} (kcal/mol)
VHH_WT	AI**RWN**G**GS**TY	GRW**DK**YG**SSF**Q**DEY**DY	3190	12800	79.3	81.7	-10.2	-10.70
VHH_h1	..GPF.YE..	...NR..FED..NF..	14.2	5.7	86.2	86.1	☆	-13.30
VHH_h2	..SPF..N..	...NR..FED..NF..	4.5	4.6	89.6	89.5	☆	-13.31
VHH_h3	..GPF..T..	...NR..EQD.YN.E.	37.6	13.5	91.0	90.2	☆	-13.75
VHH_h4	..GPF..H..	...NR..FYD..N...	5.6	4.8	90.0	88.7	☆	-14.70
VHH_h5	..GPF.....	...NR..FED..NF..	4.1	2.8	85.8	85.2	☆	-12.89

(Note: CDR definition: AbM, ☆ means it was not denatured under the most extreme conditions)

Table S7. Crystallization data.

Protein complex	**hVsig4-VHH_h1**	**hVsig4-VHH_h2**	**hVsig4-VHH_h3**	**hVsig4-VHH_h4**	**hVsig4-VHH_h5**
Crystallization conditions	0,17M ammonium sulfate 15% glycerol 25,5% PEG 4000	0,1M Na-citrate pH 5,6 20% 2-propanol 21% PEG 4000	0,1M Na-citrate pH 5,6 20% 2-propanol 21% PEG 4000	0,1M Bis-Tris pH 6.0 24% PEG3350	0,1M Bis-Tris pH 6.5 30% PEG3350
Temperature (K)	287	287	294	293	293
Protein concentration (mg/ml)	4,2	4,2	5,6	3,80	4,5
Cryoprotectant	none	25% ethylene glycol	20% ethylene glycol	15% glycerol	15% glycerol
Data collection[a]					
X-ray source	PETRA III (P13)	PETRA III (P13)	PETRA III (P13)	ALBA (Xaloc)	ALBA (Xaloc)
Space group	$P2_12_12_1$	$P2_12_12_1$	$P2_12_12_1$	$P2_12_12_1$	$P2_12_12_1$
Cell dimensions					
a, *b*, *c* (Å)	50.651, 51.404, 89.649	52.291 53.069 87.531	60.867 129.940 144.280	25.7, 51.0, 175.2	25.7, 50.9, 175.9
α, β, γ (°)	90.0, 90.0, 90.0	90.0, 90.0, 90.0	90.0, 90.0, 90.0	90.0, 90.0, 90.0	90.0, 90.0, 90.0
Unique reflections	109581 (17482)	43885 (7006)	89487 (14083)	18076 (928)	17284 (825)
Wavelenght (Å)	0.9762	0.9762	0.9762	0.9793	0.9793
Resolution (Å)	51.40–1.05 (1.11-1.05)	53.07-1.45 (1.54-1.45)	129.94-1.90 (2.01-1.90)	87.62-1.94 (1.97-1.94)	87.95-1.97 (2.00-1.97)
R_{meas} (%)	10.0 (102.8)	8.8 (218.6)	19.8 (247.1)	9.6 (109.4)	11.3 (99.2)
$<I/\sigma>$	12.40 (1.59)	17.77 (1.13)	13.61 (1.19)	16.0 (2.5)	13.5 (2.4)
Completeness (%)	99.90 (99.42)	99.90 (100)	98.3 (97.1)	100 (100)	100 (100)
Redundancy	13.3 (11.9)	13.3 (13.3)	13.9 (13.5)	12.6 (12.8)	12.5 (12.3)
CC (½) (%)	99.7 (75.7)	100 (42.3)	99.8 (45.6)	99.8 (91.0)	99.8 (90.9)
Wilson B factor (Å^2)	15.02	27.10	36.57	31.67	31.15
Refinement[b]					
Resolution (Å)	24.71 - 1.05 (1.06 - 1.05)	33.56 - 1.45 (1.502 - 1.45)	64.97 – 1.90 (1.92 – 1.90)	44.05-1.94 (2.009-1.94)	44.04-1.97 (2.04-1.97)
No. reflections	109570 (10760)	43876 (4327)	89397 (8824)	17989 (1772)	17159 (1630)
R_{work} (%)	15.67	17.34	19.08	19.63	19.75
R_{free} (%)	17.57	21.51	22.83	24.01	24.30
No. non-H atoms	2328	2162	8376	2060	1985
Protein	2069	1948	7810	1937	1918
Ligand/ion	5	36	47	6	-
Water	254	178	519	117	67
B-factors (Å^2)	20.06	27.74	35.86	54.69	48.46
Protein	18.42	26.52	35.62	54.99	48.61
Ligand/ion	17.25	40.08	47.68	49.02	-
Water	33.45	38.61	38.35	49.97	44.27
R.m.s. deviations					
Bond lengths (Å)	0.012	0.002	0.007	0.008	0.009
Bond angles (°)	1.25	0.65	0.87	1.07	1.06
Ramachandran favored (%)	97.52	96.64	96.79	95.3	95.3
Ramachandran allowed (%)	2.48	3.36	3.21	4.7	4.7
Ramachandran outliers (%)	0	0	0	0	0
PDB ID	9EZU	9EZV	9EZW	9EZH	9EZI

[a] Each data set was collected from a single crystal. Values in parentheses correspond to the highest resolution shell. Values reported by XDS.
[b] Values reported by Phenix

Table S8.
Interactions at the VHH_WT:hVSIG4 interfaces compared to the interactions at the VHH_h:hVSIG4 interfaces.

hVsig4:VHH_WT interface (5IML)							
Van der Waals contacts		Potential H-bonds			Potential salt bridges		
hVsig4	VHH_WT	hVsig4	VHH_WT		hVsig4		VHH_WT
Ile 3	**CDR1:**			**CDR3:**			**CDR3**
Pro 7	Thr 27	Ile 111	-	Arg 99	Glu 95	-	Lys 102
Glu 8	Ser 29	Val 6	-	Arg 99	Arg 108	-	Glu 110
Lys 36	Ser 30	Val 6	-	Arg 99			
Leu 38	Tyr 31	Asp 109	-	Asp 101			
Gln 40	**CDR2:**	Asp 109	-	Lys 102			
Ser 43	Arg 51	Asp 109	-	Tyr 103			
Asp 44	Trp 52						
Pro 45	Asn 53						
His 91	**CDR3:**						
Thr 93	Trp 100						
Val 107	Gly 104						
Lys 110	Phe 107						
Glu 113	Asp 109						
	Glu 110						
	Tyr113						

hVsig4:VHH_h1 interface							
Van der Waals contacts		Potential H-bonds			Potential salt bridges		
hVsig4	VHH_h1	hVsig4	VHH_h1		hVsig4		VHH_h1
Ile 3	**CDR1:**			**CDR1:**			**CDR1:**
Pro 7	Thr 27	Glu 8	-	Arg 26	Glu 8	-	Arg 26
Leu 38	Ser 30						**CDR3**
Gly 42	Tyr 31			**CDR3:**	Ile 111	-	Arg 99
Ser 43	**CDR2:**	Ile 111	-	Arg 99	Glu 95	-	Arg 102
Pro 45	Pro 52	Val 6	-	Arg 99	Arg 108	-	Asp 107
His 91	Phe 53	Gln 40	-	Asn 101	Arg 1	-	Asp 107
Val 107	Gly 54	Thr 93	-	Asn 101	Arg 1	-	Asp 109
Lys 110	Glu 56	Glu 95	-	Arg 102			
	CDR3:	Asp 109	-	Asn 101			
	Trp 100	Asp 109	-	Arg 102			
	Gly 104	Asp 109	-	Tyr 103			
	Asn 110	Arg 108	-	Asp 107			
	Asp 112	Arg 1	-	Asp 107			
		Arg 1	-	Asp 109			

hVsig4:VHH_h2 interface							
Van der Waals contacts		Potential H-bonds			Potential salt bridges		
hVsig4	VHH_h2	hVsig4	VHH_h2		hVsig4		VHH_h2
Ile 3	**CDR1:**			**CDR1:**			**CDR3**
Pro 7	Ser 30	Glu 8	-	Thr 27	Glu 95	-	Arg 102
Leu 38	**CDR2:**	Glu 8	-	Tyr 31	Arg 108	-	Asp 107
Gly 42	Pro 52			**CDR3:**	Arg 1	-	Asp 107
Ser 43	Phe 53	Ile 111	-	Arg 99	Arg 1	-	Asp 109
Pro 45	Gly 54	Val 6	-	Arg 99			
His 91	Glu 56	Gln 40	-	Asn 101			
Val 107	**CDR3:**	Thr 93	-	Asn 101			
Lys 110	Trp 100	Glu 95	-	Arg 102			
	Gly 104	Asp 109	-	Asn 101			
	Asn 110	Asp 109	-	Arg 102			
	Asp 112	Asp 109	-	Tyr 103			
		Arg 108	-	Asp 107			
		Arg 1	-	Asp 107			
		Arg 1	-	Asp 109			

hVsig4:VHH_h3 interface							
Van der Waals contacts		Potential H-bonds			Potential salt bridges		
hVsig4	VHH_h3	hVsig4	VHH_h3		hVsig4		VHH_h3
Ile 3	**CDR1:**			**CDR1:**			**CDR1**
Glu 5	Thr 27	Glu 8	-	Arg 26	Glu 8	-	Arg 26
Lys 36	Ser 30						**CDR3**
Leu 38	Tyr 31			**CDR3:**	Glu 95	-	Arg 102
Gly 42	**CDR2:**	Ile 111	-	Arg 99	Arg 108	-	Asp 107
Ser 43	Pro 52	Val 6	-	Arg 99	Lys 110	-	Glu 112
Pro 45	Phe 53	Gln 40	-	Asn 101			
His 91	Gly 54	Thr 93	-	Asn 101			
Val 107	**CDR3:**	Glu 95	-	Arg 102			
Glu 113	Trp 100	Asp 109	-	Arg 102			
Arg 115	Gly 104	Asp 109	-	Tyr 103			
	Tyr 109	Arg 108	-	Asp 107			
	Tyr 113	Lys 110	-	Asn 110			
		Lys 110	-	Glu 112			

hVsig4:VHH_h4 interface							
Van der Waals contacts		Potential H-bonds			Potential salt bridges		
hVsig4	VHH_h4	hVsig4	VHH_h4		hVsig4		VHH_h4
Ile 3	**CDR1:**			**CDR1:**			**CDR1**
Lys 36	Ser 30	Glu 8	-	Arg 26	Glu 8	-	Arg 26
Leu 38	Tyr 31						**CDR3**
Gly 42	**CDR2:**			**CDR3:**	Glu 95		Arg 102
Ser 43	Phe 53	Ile 111	-	Arg 99	Arg 1	-	Asp 107
Pro 45	Pro 52	Val 6	-	Arg 99	Arg 108	-	Asp 107
His 91	Gly 54	Val 6	-	Arg 99	Arg 1	-	Asp 109
Val 106	Gly 55	Gln 40	-	Asn 101		-	
Val 107	**CDR3:**	Thr93	-	Asn 101			
Lys 110	Trp 100	Asp 109	-	Asn 101			
	Gly 104	Glu 95	-	Arg 102			
	Asn 110	Asp 109	-	Arg 102			
	Asp 112	Asp 109	-	Tyr 103			
		Arg 108	-	Tyr 106			
		Arg 1	-	Asp 107			
		Arg 108	-	Asp 107			
		Arg 1	-	Asp 109			

hVsig4:VHH_h5 interface							
Van der Waals contacts		Potential H-bonds			Potential salt bridges		
hVsig4	VHH_h5	hVsig4	VHH_h5		hVsig4		VHH_h5
Ile 3	**CDR1:**			**CDR1:**			**CDR1**
Lys 36	Ser 30	Glu 8	-	Tyr 31	Glu 8	-	Arg 26
Leu 38	**CDR2:**			**CDR3:**			**CDR3**
Gly 42	Pro 52	Ile 111	-	Arg 99	Glu 95	-	Arg 102
Ser 43	Phe 53	Val 6	-	Arg 99	Arg 1	-	Asp 107
Pro 45	Gly 54	Pro 7	-	Arg 99	Arg 108	-	Asp 107
His 91	**CDR3:**	Gln 40	-	Asn 101	Arg 1	-	Asp 109
Val 107	Trp 100	Thr93	-	Asn 101			
	Gly 104	Asp 109	-	Asn 101			
	Asp 112	Glu 95	-	Arg 102			
	Tyr 113	Asp 109	-	Arg 102			
		Asp 109	-	Tyr 103			
		Arg 1	-	Asp 107			
		Arg 108	-	Asp 107			
		Arg 1	-	Asp 109			
		Lys 110	-	Asn 101			

References

1. G. Pantaleo, B. Correia, C. Fenwick, V. S. Joo, L. Perez, Antibodies to combat viral infections: development strategies and progress. *Nat Rev Drug Discov* **21**, 676-696 (2022).
2. S. Modi *et al.*, Trastuzumab Deruxtecan in Previously Treated HER2-Low Advanced Breast Cancer. *N Engl J Med* **387**, 9-20 (2022).
3. A. Mullard, 2023 FDA approvals. *Nat Rev Drug Discov* **23**, 88-95 (2024).
4. J. Kim, M. McFee, Q. Fang, O. Abdin, P. M. Kim, Computational and artificial intelligence-based methods for antibody development. *Trends Pharmacol Sci* **44**, 175-189 (2023).
5. P. Sormanni, F. A. Aprile, M. Vendruscolo, Third generation antibody discovery methods: in silico rational design. *Chem Soc Rev* **47**, 9137-9157 (2018).
6. A. K. Kiani *et al.*, Ethical considerations regarding animal experimentation. *J Prev Med Hyg* **63**, E255-e266 (2022).
7. N. R. Bennett *et al.*, Atomically accurate de novo design of single-domain antibodies, bioRxiv 2024.2003.2014.585103 [Preprint] (2024).https://doi.org/10.1101/2024.03.14.585103.
8. R. R. Eguchi *et al.*, Deep Generative Design of Epitope-Specific Binding Proteins by Latent Conformation Optimization, bioRxiv 2022.2012.2022.521698 [Preprint] (2022).https://doi.org/10.1101/2022.12.22.521698.
9. S. Luo *et al.*, Antigen-Specific Antibody Design and Optimization with Diffusion-Based Generative Models for Protein Structures, bioRxiv 2022.2007.2010.499510 [Preprint] (2022).https://doi.org/10.1101/2022.07.10.499510.
10. A. Shanehsazzadeh *et al.*, Unlocking *de novo* antibody design with generative artificial intelligence, bioRxiv 2023.2001.2008.523187 [Preprint] (2024).https://doi.org/10.1101/2023.01.08.523187.
11. G. D. Lapidoth *et al.*, AbDesign: An algorithm for combinatorial backbone design guided by natural conformations and sequences. *Proteins* **83**, 1385-1406 (2015).
12. A. M. Hummer, B. Abanades, C. M. Deane, Advances in computational structure-based antibody design. *Curr Opin Struct Biol* **74**, 102379 (2022).
13. J. Adolf-Bryfogle *et al.*, RosettaAntibodyDesign (RAbD): A general framework for computational antibody design. *PLoS Comput Biol* **14**, e1006112 (2018).
14. M. Baek *et al.*, Accurate prediction of protein structures and interactions using a three-track neural network. *Science* **373**, 871-876 (2021).
15. G. Nimrod *et al.*, Computational Design of Epitope-Specific Functional Antibodies. *Cell Rep* **25**, 2121-2131 e2125 (2018).
16. D. Cianferoni, L. G. Radusky, S. A. Head, L. Serrano, J. Delgado, ProteinFishing: a protein complex generator within the ModelX toolsuite. *Bioinformatics* **36**, 4208-4210 (2020).
17. A. Montero-Blay *et al.*, Bacterial expression of a designed single-chain IL-10 prevents severe lung inflammation. *Mol Syst Biol* **19**, e11037 (2023).
18. J. D. Blanco, L. Radusky, H. Climente-Gonzalez, L. Serrano, FoldX accurate structural protein-DNA binding prediction using PADA1 (Protein Assisted DNA Assembly 1). *Nucleic Acids Res* **46**, 3852-3863 (2018).

19. J. Schymkowitz *et al.*, The FoldX web server: an online force field. *Nucleic Acids Res* **33**, W382-388 (2005).
20. A. M. Fernandez-Escamilla, F. Rousseau, J. Schymkowitz, L. Serrano, Prediction of sequence-dependent and mutational effects on the aggregation of peptides and proteins. *Nat Biotechnol* **22**, 1302-1306 (2004).
21. R. Linding, J. Schymkowitz, F. Rousseau, F. Diella, L. Serrano, A comparative study of the relationship between protein structure and beta-aggregation in globular and intrinsically disordered proteins. *J Mol Biol* **342**, 345-353 (2004).
22. F. Rousseau, J. Schymkowitz, L. Serrano, Protein aggregation and amyloidosis: confusion of the kinds? *Curr Opin Struct Biol* **16**, 118-126 (2006).
23. Y. Wen *et al.*, Structural evaluation of a nanobody targeting complement receptor Vsig4 and its cross reactivity. *Immunobiology* **222**, 807-813 (2017).
24. A. Vuchelen *et al.*, (1)H, (13)C and (15)N assignments of a camelid nanobody directed against human alpha-synuclein. *Biomol NMR Assign* **3**, 231-233 (2009).
25. Y. Nie *et al.*, Chemical shift assignments of a camelid nanobody against aflatoxin B(1). *Biomol NMR Assign* **13**, 75-78 (2019).
26. M. Percipalle, Y. Hunashal, J. Steyaert, F. Fogolari, G. Esposito, Structure of Nanobody Nb23. *Molecules* **26**, (2021).
27. T. D. Vos *et al.*, Structural basis for the mechanism and antagonism of receptor signaling mediated by Interleukin-9 (IL-9), bioRxiv 2022.2012.2030.522308 [Preprint] (2022).https://doi.org/10.1101/2022.12.30.522308.
28. M. Varadi *et al.*, AlphaFold Protein Structure Database: massively expanding the structural coverage of protein-sequence space with high-accuracy models. *Nucleic Acids Res* **50**, D439-D444 (2022).
29. A. Shimbara *et al.*, IL-9 and its receptor in allergic and nonallergic lung disease: increased expression in asthma. *J Allergy Clin Immunol* **105**, 108-115 (2000).
30. K. Verstraete *et al.*, Efficient production of bioactive recombinant human Flt3 ligand in E. coli. *The protein journal* **28**, 57-65 (2009).
31. E. Pardon *et al.*, A general protocol for the generation of Nanobodies for structural biology. *Nat Protoc* **9**, 674-693 (2014).
32. L. Rue *et al.*, Novel Human/Non-Human Primate Cross-Reactive Anti-Transferrin Receptor Nanobodies for Brain Delivery of Biologics. *Pharmaceutics* **15**, (2023).
33. W. Kabsch, Xds. *Acta Crystallogr D Biol Crystallogr* **66**, 125-132 (2010).
34. C. Vonrhein *et al.*, Data processing and analysis with the autoPROC toolbox. *Acta Crystallogr D Biol Crystallogr* **67**, 293-302 (2011).
35. L. Cao *et al.*, Design of protein-binding proteins from the target structure alone. *Nature* **605**, 551-560 (2022).
36. P. Emsley, K. Cowtan, Coot: model-building tools for molecular graphics. *Acta Crystallogr D Biol Crystallogr* **60**, 2126-2132 (2004).
37. G. N. Murshudov, A. A. Vagin, E. J. Dodson, Refinement of macromolecular structures by the maximum-likelihood method. *Acta Crystallogr D Biol Crystallogr* **53**, 240-255 (1997).
38. P. V. Afonine *et al.*, Real-space refinement in PHENIX for cryo-EM and crystallography. *Acta Crystallogr D Struct Biol* **74**, 531-544 (2018).

39. V. Y. Orekhov, V. A. Jaravine, Analysis of non-uniformly sampled spectra with multi-dimensional decomposition. *Prog Nucl Magn Reson Spectrosc* **59**, 271-292 (2011).
40. F. Delaglio *et al.*, NMRPipe: a multidimensional spectral processing system based on UNIX pipes. *J Biomol NMR* **6**, 277-293 (1995).
41. W. F. Vranken *et al.*, The CCPN data model for NMR spectroscopy: development of a software pipeline. *Proteins* **59**, 687-696 (2005).
42. M. S. Cheung, M. L. Maguire, T. J. Stevens, R. W. Broadhurst, DANGLE: A Bayesian inferential method for predicting protein backbone dihedral angles and secondary structure. *J Magn Reson* **202**, 223-233 (2010).
43. M. V. Berjanskii, D. S. Wishart, A simple method to predict protein flexibility using secondary chemical shifts. *J Am Chem Soc* **127**, 14970-14971 (2005).
44. A. M. Mandel, M. Akke, A. G. Palmer, 3rd, Backbone dynamics of Escherichia coli ribonuclease HI: correlations with structure and function in an active enzyme. *J Mol Biol* **246**, 144-163 (1995).
45. R. Cole, J. P. Loria, FAST-Modelfree: a program for rapid automated analysis of solution NMR spin-relaxation data. *J Biomol NMR* **26**, 203-213 (2003).
46. L. K. Lee, M. Rance, W. J. Chazin, A. G. Palmer, 3rd, Rotational diffusion anisotropy of proteins from simultaneous analysis of 15N and 13C alpha nuclear spin relaxation. *J Biomol NMR* **9**, 287-298 (1997).
47. J. Garcia de la Torre, M. L. Huertas, B. Carrasco, HYDRONMR: prediction of NMR relaxation of globular proteins from atomic-level structures and hydrodynamic calculations. *J Magn Reson* **147**, 138-146 (2000).